Spin-Orbit Coupling, Quantum Dots, and Qubits in Monolayer Transition Metal Dichalcogenides

Andor Kormányos,[1,*] Viktor Zólyomi,[2] Neil D. Drummond,[2] and Guido Burkard[1]

[1]*Department of Physics, University of Konstanz, D-78464 Konstanz, Germany*
[2]*Department of Physics, Lancaster University, Lancaster LA1 4YB, United Kingdom*
(Received 28 October 2013; revised manuscript received 20 December 2013; published 11 March 2014)

We derive an effective Hamiltonian that describes the dynamics of electrons in the conduction band of monolayer transition metal dichalcogenides (TMDC) in the presence of perpendicular electric and magnetic fields. We discuss in detail both the intrinsic and the Bychkov-Rashba spin-orbit coupling induced by an external electric field. We point out interesting differences in the spin-split conduction band between different TMDC compounds. An important consequence of the strong intrinsic spin-orbit coupling is an effective out-of-plane g factor for the electrons that differs from the free-electron g factor $g \simeq 2$. We identify a new term in the Hamiltonian of the Bychkov-Rashba spin-orbit coupling that does not exist in III-V semiconductors. Using first-principles calculations, we give estimates of the various parameters appearing in the theory. Finally, we consider quantum dots formed in TMDC materials and derive an effective Hamiltonian that allows us to calculate the magnetic field dependence of the bound states in the quantum dots. We find that all states are both valley and spin split, which suggests that these quantum dots could be used as valley-spin filters. We explore the possibility of using spin and valley states in TMDCs as quantum bits, and conclude that, due to the relatively strong intrinsic spin-orbit splitting in the conduction band, the most realistic option appears to be a combined spin-valley (Kramers) qubit at low magnetic fields.

Subject Areas: Condensed Matter Physics, Nanophysics, Spintronics

I. INTRODUCTION

Monolayers of transition metal dichalcogenides (TMDCs) [1] posses a number of remarkable electrical and optical properties, which makes them an attractive research platform. Their material composition can be described by the formula MX_2, where $M =$ Mo or W and $X =$ S or Se. They are atomically thin, two-dimensional materials, and in contrast to graphene [2], they have a finite direct optical band gap of approximately 1.5–2 eV, which is in the visible frequency range [3,4]. This has facilitated the theoretical [5] and experimental [6–11] study of the rich physics related to the coupling of the spin and the valley degrees of freedom.

Very recently, there has also been a growing interest in the transport properties of these materials. Although contacting and gating monolayer TMDCs is not entirely straightforward experimentally, progress is being made in this respect [12–18]. Electric [17] and magnetic field [19,20] effects are also being studied currently, in both monolayer and few-layer samples. In addition, a promising

experimental work has recently appeared regarding spin physics in these materials, showing, e.g., a viable method for spin injection from ferromagnetic contacts [16].

The finite band gap in the TMDCs should also make it possible to confine the charge carriers with external gates and, therefore, to create, e.g., quantum dots (QDs). Together with the above-mentioned progress in contacting and gating TMDCs, this raises the exciting question of whether these materials could be suitable platforms to host qubits [21]. Our work is motivated by this question.

First, we introduce an effective Hamiltonian that accurately describes the physics in the conduction band (CB) of TMDCs in the (degenerate) K and K' valleys of the Brillouin zone (BZ). We confine our attention to the CB while the effect of the valence band (VB) and other relevant bands is taken into account through an appropriate choice of the parameters appearing in the model. This approach is motivated by the facts that (i) the band-gap energy E_{bg} is large with respect to other energy scales appearing in the problem and (ii) according to experimental observations, the samples of TMDCs are often intrinsically n doped [16,22] or show unipolar n-type behavior [23]. To obtain realistic values of the parameters appearing in the theory, we perform density functional theory (DFT) calculations. We discuss the important effects of the intrinsic spin-orbit coupling (SOC) that manifest themselves through both the spin splitting of the CB and the different effective masses

*andor.kormanyos@uni-konstanz.de

associated with the spin-split bands. We also point out that a perpendicular magnetic field, in addition to the usual orbital effect, leads to the breaking of valley degeneracy. Moreover, due to the strong SOC, the coupling of the spin degree of freedom to the magnetic field is described by an out-of-plane effective g factor $\tilde{g}_{\mathrm{sp}}^{\perp}$.

We then study the effect of an external electric field and derive the Bychkov-Rashba SOC Hamiltonian for TMDCs. This is motivated by recent experiments [11,22], where strong electric fields were created by backgates to study the charged excitons. In particular, we find that in contrast to III-V semiconductors and graphene, due to the lower symmetry of the system, the Bychkov-Rashba SOC Hamiltonian contains two terms, one of which has not yet been discussed in the literature. Using perturbation theory and first-principles (FP) calculations, we estimate the magnitude of this effect for each TMDC material.

Finally, we consider QDs obtained by confining the charge carriers with gate electrodes (see Fig. 1). We study the dependence of the spectrum of such QDs on a perpendicularly applied external magnetic field. We show that, while pure spin and pure valley qubits are possible, e.g., in small QDs in MoS$_2$, they require large magnetic fields because of the relatively strong intrinsic SOC in the CB. On the other hand, combined spin-valley qubits represented by a Kramers pair can be operated at small magnetic fields. QDs in nanowires consisting of a MoS$_2$ nanoribbon with armchair edges or crystallographically aligned confining gates have recently been discussed [24]. Our proposal does not require atomically sharp boundaries or a precise control of the placement of the confining gates; therefore, it should be easier to fabricate experimentally. Moreover, we explicitly take into account the intrinsic spin splitting of the CB.

The paper is organized as follows. In Sec. II, we derive an effective Hamiltonian describing electrons in the CB. We take into account the effects of perpendicular external electric and magnetic fields. Using the results of FP calculatio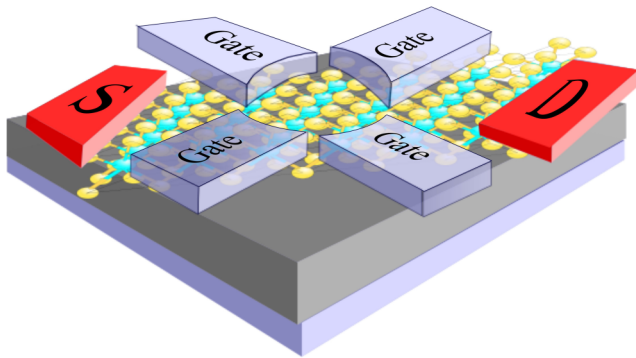ns, we obtain values for the important parameters appearing in our model. In Sec. III, we use this model to study the magnetic field dependence of the bound states in a QD. We also discuss the possible types of qubits that QDs in TMDCs can host. We conclude in Sec. IV. In Appendixes A and B, we present the details of the derivation of the effective Hamiltonian. We collect some useful formulas in Appendix C, and the details of our DFT calculations can be found in Appendix D.

II. EFFECTIVE HAMILTONIAN

We consider a monolayer TMDC and introduce a low-energy effective Hamiltonian that captures the most important effects in the spin-split conduction band at the K (K') point. The detailed derivation of the model, which is based on a seven-band (without the spin degree of freedom) $\mathbf{k} \cdot \mathbf{p}$ Hamiltonian, is presented in Appendix A. It is important to note that, as pointed out in Refs. [25–27], there are several band extrema in the band structure of TMDCs that can be of importance: see Fig. 2, where we show the band structure of MoS$_2$ obtained from DFT calculations. Since we assume that the system is n doped, the maximum at the Γ point of the VB is not relevant. More important are the secondary minima in the CB, which are usually called the Q (or T) points. The exact alignment of the Q-point energy minimum with respect to the K-point minimum is difficult to deduce from DFT and GW calculations, because it depends quite sensitively on the details of these computations [28]. We found that by using the local density approximation (LDA), all compounds, with the exception of MoS$_2$, become indirect gap semiconductors if we take into account the SOC, because the Q-point minimum is lower than the K-point minimum. More advanced GW calculations also give somewhat conflicting results and are quite sensitive to the level of theory [29] (G_0W_0, GW_0, etc,) and the lattice constant used. Experimentally, monolayer TMDCs show a significant increase of photoluminescence [10,22,30,31] with respect to few-layer or bulk TMDCs, which is usually

FIG. 1   Schematics of a QD defined with the help of four top gates in a monolayer TMDC. S and D denote the source and the drain, respectively.
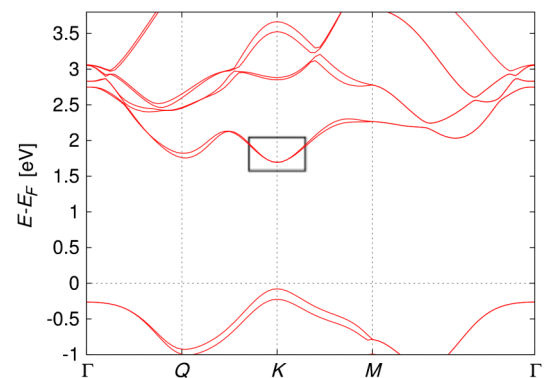
FIG. 2   Spin-resolved band structure of MoS$_2$ from DFT calculations. The qualitative features of the band structure are the same for all TMDCs. An enlargement of the region in the black frame is shown in the upper panel of Fig. 3.

interpreted as evidence that they are direct gap semiconductors. Therefore, we assume that for low densities it is enough to consider only the K and K' points of the CB. For the formation of QDs from states around the K point, the safest material appears to be MoS_2, where the secondary minima are most likely above the K-point minimum by a few hundred meV [26,32]. However, for operation at low temperatures, the other TMDCs may also be suitable, as long as the Q point lies a few meV higher than the K points. In cases where the Q point lies below the K point, one can envisage QDs formed within the Q valley, but this is beyond the scope of this paper.

A. Electronic part and intrinsic spin-orbit coupling

Because of the absence of a center of inversion and strong SOC, the bands of monolayer TMDC materials are spin split everywhere in the BZ except at the high-symmetry points Γ and M, where the bands remain degenerate. In addition, the projection of the spin onto the quantization axis perpendicular to the plane of the monolayer is also preserved. This is a consequence of another symmetry, namely, the presence of a horizontal mirror plane σ_h. Therefore, a suitable basis to describe the CB is given by the eigenstates $\uparrow$ and $\downarrow$ of the dimensionless spin Pauli matrix s_z with eigenvalues $s = \pm 1$. In what follows, we often use the shorthand notation $\uparrow$ for $s = 1$ and $\downarrow$ for $s = -1$.

In the absence of external magnetic and electric fields, the effective low-energy Hamiltonian that describes the spin-split CB at the K (K') point in the basis $\uparrow, \downarrow$ is

$$\tilde{H}_{\mathrm{el}}^{\tau,s} + \tilde{H}_{\mathrm{so}}^{\mathrm{intr}} = \frac{\hbar^2 q_+ q_-}{2m_{\mathrm{eff}}^{\tau,s}} + \tau \Delta_{\mathrm{CB}} s_z. \tag{1}$$

Here, we introduce the inverse effective mass $\frac{1}{m_{\mathrm{eff}}^{\tau,s}} = \frac{1}{m_{\mathrm{eff}}^0} - \tau s \frac{1}{\delta m_{\mathrm{eff}}}$, where $\tau = 1 \ (-1)$ for K (K') and the wave numbers $q_\pm = q_x \pm i q_y$ are measured from the K (K') point. Leaving the discussion of the effects of a magnetic field to Sec. II B, we set $q_+ q_- = q_x^2 + q_y^2$, and, therefore, the dispersion described by the Hamiltonian [Eq. (1)] is parabolic and isotropic. The trigonal warping [26], which is much more pronounced in the VB than in the CB, is neglected here.

The strong spin-orbit coupling in TMDCs has two consequences. First, as already mentioned, the CB is spin split at the K (K') point, and this is described by the parameter Δ_{CB}. Second, the effective mass is different for the $\uparrow$ and $\downarrow$ bands. Our sign convention for the effective mass assumes that the spin-up band is heavier than the spin-down band at the K point (for details on the effective mass calculations, see Appendix B). The effective mass $m_{\mathrm{eff}}^{K,s}$ of different TMDCs, obtained from fitting the DFT band structure [33], is shown in Table I (note that $m_{\mathrm{eff}}^{K',s} = m_{\mathrm{eff}}^{K,-s}$). As one can see, the difference between $m_{\mathrm{eff}}^{K,\uparrow}$ and $m_{\mathrm{eff}}^{K,\downarrow}$ is around 10%–14% for MoS_2 and $MoSe_2$,

TABLE I. Effective masses and CB spin splittings appearing in the Hamiltonian [Eq. (1)] for different TMDCs. m_e is the free-electron mass.

	MoS_2	WS_2	$MoSe_2$	WSe_2
$m_{\mathrm{eff}}^{K,\uparrow}/m_e$	0.49	0.35	0.64	0.4
$m_{\mathrm{eff}}^{K,\downarrow}/m_e$	0.44	0.27	0.56	0.3
$2\Delta_{\mathrm{CB}}$ [meV]	3	−38	23	−46

while it is $\gtrsim 30\%$ for the WX_2 compounds. In the seven-band $\mathbf{k} \cdot \mathbf{p}$ model, this can be explained by the fact that the effective mass depends on the ratio of the spin splittings in other bands (most importantly, in the VB and the second band above the CB) and the band gap E_{bg}. For the heavier compounds, the spin splittings are larger, but E_{bg} remains roughly the same or even decreases, leading to a larger difference in the effective masses.

The results of DFT calculations also suggest that, in the case of MoX_2 materials, there are band crossings between the spin-split CB because the heavier band has higher energy. For WX_2 materials, such a band crossing is absent. Taking MoS_2 and WS_2 as an example, the dispersion in the vicinity of the K point is shown in Fig. 3. A similar figure could be obtained for $MoSe_2$ and WSe_2 as well, except that, due to the larger spin splitting, the band crossings for
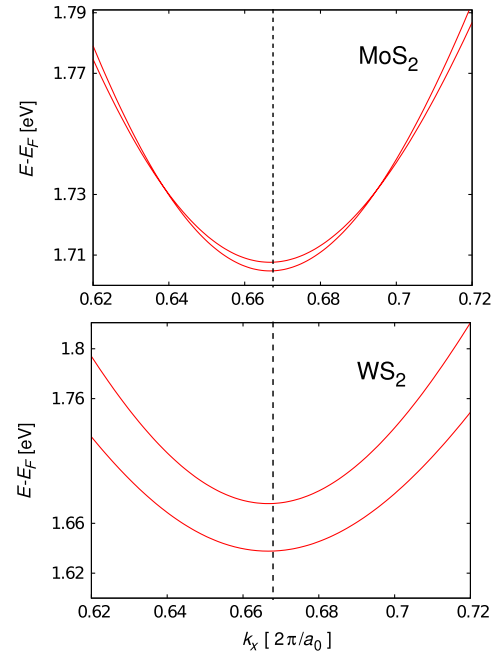

FIG. 3   Upper panel: Spin-split DFT CB of MoS_2 in the vicinity of the K point, which is indicated by a vertical dashed line. Lower panel: The same for WS_2. A band crossing, which can be seen in the case of MoS_2, is absent for WS_2. The small asymmetry in the figures with respect to the K point, especially in the case of the band-crossing points in the upper panel, is due to the fact that the calculations were performed along the ΓKM line.

MoSe$_2$ occur farther away from the K point. Within the present model, which focuses on the CB, such a different behavior can be accounted for by a different sign of Δ_{CB} for MoX$_2$ and WX$_2$ materials. A discussion about the possible microscopic origin of this sign difference is presented in Appendix B.

We note that a model Hamiltonian similar to Eq. (1), but without taking into account the difference in the effective masses, was used in Refs. [34,35] to study spin-relaxation processes in MoS$_2$. The effective mass difference and the sign of the effective SOC in the CB was discussed recently in Ref. [36].

B. Effects of a perpendicular magnetic field

We assume that a homogeneous, perpendicular magnetic field of strength B_z is applied. The $\mathbf{k} \cdot \mathbf{p}$ Hamiltonian can be obtained by using the Kohn-Luttinger prescription, which amounts to replacing the numbers q_x and q_y in the above formulas with operators $\mathbf{q} \to \hat{\mathbf{q}} = \frac{1}{i}\nabla + \frac{e}{\hbar}\mathbf{A}$, where $\mathbf{A}$ is the vector potential in Landau gauge and $e > 0$ is the magnitude of the electron charge. Note that, due to this replacement, $\hat{q}_+$ and $\hat{q}_-$ become noncommuting operators, $[\hat{q}_-, \hat{q}_+] = \frac{2eB_z}{\hbar}$, where $|B_z|$ is the strength of the magnetic field. Therefore, their order has to be preserved when one folds down a multiband Hamiltonian, which lies behind the low-energy effective Hamiltonian [Eq. (1)]. As a consequence, for a finite magnetic field, further terms appear in the effective Hamiltonian. The derivation of these terms within a seven-band $\mathbf{k} \cdot \mathbf{p}$ model is given in Appendix B.

One finds that in an external magnetic field $H_{el}^{\tau,s}$ in Eq. (1) is replaced by

$$\tilde{H}_{el}^{\tau,s} + \tilde{H}_{vl}^{\tau} + \tilde{H}_{sp}^{s} = \frac{\hbar^2\hat{q}_+\hat{q}_-}{2m_{eff}^{\tau,s}} + \frac{1+\tau}{2}\mathrm{sgn}(B_z)\hbar\omega_c^{\tau,s}$$
$$- \frac{\tau}{2}\tilde{g}_{vl}\mu_B B_z + \frac{1}{2}\mu_B g_{so}^{\perp}s_z B_z, \quad (2)$$

where $\hbar\omega_c^{\tau,s} = e|B_z|/m_{eff}^{\tau,s}$.

The term $\sim\omega_c^{\tau,s}$ in the bulk case introduces a shift in the index of the Landau levels, so that there is an "unpaired" lowest Landau level in one of the valleys. The next term, $\tilde{H}_{vl}^{\tau} = -\tau\tilde{g}_{vl}\mu_B B_z$, breaks the valley symmetry of Landau levels. Here $\tilde{g}_{vl}$ is the valley g factor. Similar effects have also been found in gapped monolayer [37] and bilayer [38,39] graphene, and have recently been noted for MoS$_2$ as well [40–42]; therefore, we do not discuss them here in detail.

A new term, that to our knowledge has not yet been considered in the literature of monolayer TMDC, is due to the strong SOC in these materials. It can be written in terms of an out-of-plane effective spin g factor $g_{so}^{\perp}$: $\tilde{H}_{sp}^{s} = \frac{1}{2}g_{so}^{\perp}\mu_B s_z B_z$, where μ_B is the Bohr magneton. In addition, the well-known Zeeman term $H_Z = \frac{1}{2}g_e\mu_B s_z B_z$

TABLE II. Valley ($\tilde{g}_{vl}$, g_{vl}) and spin ($g_{so}^{\perp}$, $g_{sp}^{\perp}$) g factors for different TMDCs.

	MoS$_2$	WS$_2$	MoSe$_2$	WSe$_2$
$\tilde{g}_{vl}$	3.57	4.96	3.03	4.34
$|g_{so}^{\perp}|$	0.21	0.84	0.29	0.87
g_{vl}	0.75	1.6	0.42	1.46
$g_{sp}^{\perp}$	1.98	1.99	2.07	2.04

also has to be taken into account [43]. Here, $g_e \approx 2$ is the free-electron g factor. The coupling of the spin to the magnetic field can, therefore, be described by

$$\tilde{H}_{sp,tot}^{s} = \frac{1}{2}\tilde{g}_{sp}^{\perp}\mu_B s_z B_z, \quad (3)$$

where the total g factor in the CB is $\tilde{g}_{sp}^{\perp} = g_e + g_{so}^{\perp}$. Values of $\tilde{g}_{vl}$ and $|g_{so}^{\perp}|$ obtained with the help of our DFT calculations are shown Table II. The sign of $g_{so}^{\perp}$ cannot be obtained with our methods; it should be deduced either from experiments or from more advanced FP calculations. For the numerical calculations in Sec. III A, we assume that $g_{so}^{\perp} > 0$.

In Sec. III A, we study the interplay of the magnetic field and the quantization due to confinement in QDs. While Eq. (4) is a convenient starting point to understand the Landau level physics, for relatively weak magnetic fields, when the effect of the confinement potential is important with respect to orbital effects due to the magnetic field, one may rewrite $\tilde{H}_{el}^{\tau,s}$, $\tilde{H}_{vl}^{\tau}$, and $\tilde{H}_{sp,tot}^{s}$ in a slightly different form:

$$H_{el}^{\tau,s} + H_{vl}^{\tau} + H_{sp,tot}^{s} = \frac{\hbar^2\hat{q}_+\hat{q}_-}{2m_{eff}^{\tau,s}} + \frac{1}{2}\mathrm{sgn}(B_z)\hbar\omega_c^{\tau,s}$$
$$+ \frac{\tau}{2}g_{vl}\mu_B B_z + \frac{1}{2}\mu_B g_{sp}^{\perp}s_z B_z, \quad (4)$$

where $g_{vl} = (2m_e/m_{eff}^0) - \tilde{g}_{vl}$ and $g_{sp}^{\perp} = \tilde{g}_{sp}^{\perp} - (2m_e/\delta m_{eff})$. This form shows explicitly that, in contrast to $H_{el}^{\tau,s}$, which depends on the product of τ and s (through $m_{eff}^{\tau,s}$), H_{vl}^{τ} and $H_{sp,tot}^{s}$ depend only on τ and s_z, respectively. This can help to understand the level splittings patterns in QDs: see Sec. III A. In particular, for states that form a Kramers pair, $\tau \cdot s = 1$ or -1; therefore, $H_{el}^{\tau,s}$, which depends only on the product of τ and s, would not lift their degeneracy in the presence of a magnetic field. Because of $\tilde{H}_{vl}^{\tau}$, however, the degeneracy of the Kramers pair states will be lifted. Assuming $g_{so}^{\perp} > 0$ and $B_z > 0$, as in the calculations that lead to Figs. 4 and 5, the values of g_{vl} and $g_{sp}^{\perp}$ are shown in Table II.

C. External electric field and the Bychkov-Rashba SOC

The effective Hamiltonian [Eq. (1)] describing the dispersion and the spin splitting of the CB is diagonal in

spin space. An external electric field has two effects: (i) it can induce Bychkov-Rashba– type SOC, which will couple the different spin states, and (ii) it can change the energy of the band edge. We start with the discussion of the Bychkov-Rashba SOC.

For simplicity, we assume that the external electric field is homogeneous and that its strength is given by E_z. Then, the Bychkov-Rashba SOC in TMDCs is described by the Hamiltonian

$$\tilde{H}_{BR}^{\tau} = \lambda_{BR}^i(s_y q_x - s_x q_y) + \lambda_{BR}^r(s_x q_x + s_y q_y)$$
$$= \begin{pmatrix} 0 & \lambda_{BR}^* q_- \\ \lambda_{BR} q_+ & 0 \end{pmatrix}. \qquad (5)$$

The first term, $\lambda_{BR}^i(s_y q_x - s_x q_y)$, is the well-known Bychkov-Rashba [44] Hamiltonian, which is also present in GaAs and other III-V semiconductor compounds. It is equivalent to the Bychkov-Rashba Hamiltonian recently discussed in Ref. [45] in the framework of an effective two-band model, which includes the VB. The second term, $\lambda_{BR}^r(s_x q_x + s_y q_y)$, is also allowed by symmetry (see Table I of Ref. [46]) because the pertinent symmetry group at the K point in the presence of an external electric field is C_3. A derivation of the Hamiltonian [Eq. (5)] is given in Appendixes A and B. We note that the coupling constants λ_{BR}^r and λ_{BR}^i cannot be tuned independently, because both of them are proportional to the electric field but with different proportionality factors. Using our microscopic model and FP calculations similar to those in Ref. [47], we can estimate the magnitude of λ_{BR} but not λ_{BR}^r and λ_{BR}^i separately. The $|\lambda_{BR}|$ values that we have obtained are shown in Table III. They give an upper limit for the real values because we have neglected, e.g., screening in these calculations (for details see Appendix B). More advanced DFT calculations, such as those recently done for bilayer graphene [48], would certainly be of interest here.

Comparing the numbers shown in Table III to the values found in InAs [49] or InSb [50], one can see that, for relatively small values of the electric field ($E_z \lesssim 10^{-2}$ V/Å), where the perturbation theory approach can be expected to work, $|\lambda_{BR}|$ is smaller by an order of magnitude than in these semiconductor quantum wells. Nevertheless, the Bychkov-Rashba SOC is important because it constitutes an intravalley spin-relaxation channel, which does not require the simultaneous flip of spin *and* valley. Thus, it may play a role in the quantitative understanding of the relaxation processes in the recent

experiment of Jones *et al.* [11], where a large backgate voltage was used.

The external electric field has a further effect, which, however, turns out to be less important for our purposes. Namely, it shifts up the band edge of the CB, and the shift is, in principle, spin dependent [see Eqs. (B2c) and (B3c) in Appendix B]. The shift of the CB edge can be understood in terms of the electric field dependence of the band gap (we note that the band edge of the VB also depends on the electric field, and the shifts of the VB and CB edges together would describe the change of the band gap). In contrast to Ref. [40], however, in our model the shift of the band edge depends quadratically on the strength of the electric field and not linearly. We think this is due to the fact that in the model used in Ref. [40], the p orbitals of the sulfur atoms are admixed only to the CB. In fact, symmetry considerations [26,45] and our DFT calculations show that the p (or d) orbitals of the X atoms have a small weight at the K point both in the VB and in the CB. Taking this into account, as in the tight-binding model of Ref. [27], one would find that for a weak electric field regime, the dependence of the band gap is quadratic in the electric field. Moreover, both our perturbation theory and preliminary DFT results suggest that the shift of the band edge in the CB is actually very small, at least in the regime where the perturbation theory approach is applicable (see Appendix B for details). Therefore, we neglect it in the rest of the paper. The spin dependence of the band-edge shift, being a higher-order effect, is expected to be even smaller.

III. RESULTS

A. Quantum dots in TMDCs

QDs in novel low-dimensional structures, such as bilayer graphene [38,51–53] and semiconductor nanowires with strong SOC [54,55], are actively studied and the applicability of these structures for hosting qubits has also been discussed. Motivated by the interesting physics revealed in these studies, we now consider QDs in two-dimensional semiconducting TMDCs defined by external electrostatic gates (see, e.g., Fig. 1). In particular, we are interested in the magnetic field dependence of the spectrum and discuss which eigenstates can be used as two-level systems for qubits. We consider relatively small QDs that can be treated in the ballistic limit. The opposite limit, where disorder effects become important and the spectrum acquires certain universal characteristics, can be treated along the lines of Ref. [56], but this is beyond the scope of the present work.

Nevertheless, based on the findings of Sec. II A, the following observations can be made. Assuming a chaotic QD with mean level spacing $\delta = 2\pi\hbar^2/(m_{eff}A)$, where A is the area of the dot, one can see that one needs relatively small QDs in order to make δ larger than the thermal energy $k_B T$. For instance, taking a dot of radius $R \approx 40$ nm, we find for,

TABLE III.   Estimates of the Bychkov-Rashba SOC parameters $|\lambda_{BR}|$. The perpendicular electric field E_z is in units of V/Å.

	MoS$_2$	WS$_2$	MoSe$_2$	WSe$_2$
$|\lambda_{BR}|$ [eV Å]	$0.033 E_z$	$0.13 E_z$	$0.055 E_z$	$0.18 E_z$

e.g., MoS$_2$ that $\delta \approx 0.2$ meV, corresponding to $T = 2.3$ K, whereas for WS$_2$, due to its smaller effective mass, the mean level spacing is $T \approx 3.4$ K. In this respect, TMDCs with smaller m_{eff}, such as WS$_2$ and WSe$_2$, might be more advantageous. Although the required temperatures are smaller than in the case of GaAs (which has $m_{\mathrm{eff}} \approx 0.067 m_e$), they are still achievable with present-day techniques.

In the following, for simplicity, we study circular QDs because their spectrum can be obtained relatively easily and can illustrate some important features of the spectrum of more general cases. In particular, we consider QDs in MoS$_2$ and WS$_2$. The total Hamiltonian in the K, K' valleys ($\tau = \pm 1$) reads

$$H = H_{\mathrm{el}}^{\tau,s} + \tilde{H}_{\mathrm{so}}^{\mathrm{intr}} + \tilde{H}_{\mathrm{BR}}^{\tau} + H_{\mathrm{vl}}^{\tau} + H_{\mathrm{sp,tot}} + V_{\mathrm{dot}}, \quad (6)$$

where V_{dot} is the confinement potential for the QD. As we have shown, $\tilde{H}_{\mathrm{BR}}^{\tau}$ is relatively small; therefore, we treat it as a perturbation, whereas the stronger intrinsic SOI is treated exactly. The Hamiltonian of the nonperturbed system is given by

$$H_{\mathrm{dot}} = H_{\mathrm{el}}^{\tau,s} + H_{\mathrm{so}}^{\mathrm{intr}} + H_{\mathrm{vl}}^{\tau} + H_{\mathrm{sp,tot}} + V_{\mathrm{dot}}; \quad (7)$$

i.e., it is diagonal both in valley and in spin space. We consider a circular QD with hard-wall boundary conditions: $V_{\mathrm{dot}}(r) = 0$ for $r \leq R_d$ and $V_{\mathrm{dot}}(r) = \infty$ if $r > R_d$. In cylindrical coordinates, the perpendicular magnetic field can be taken into account using the axial gauge, where $A_\phi = B_z r/2$ and $A_r = 0$. With this choice, since the rotational symmetry around the z axis is preserved, H_{dot} commutes with the angular momentum operator $\hat{l}_z$ and they have common eigenfunctions. The Schrödinger equation, which determines the bound state energies and eigenfunctions, can be solved by making use of the fact that, as noted in Ref. [57], the operator $\hat{q}_+$ ($\hat{q}_-$) appearing in H_{el}^{τ} acts as a raising (lowering) operator on a suitably chosen trial function. Introducing the dimensionless new variable, $\rho = \frac{1}{2}(\frac{r}{l_B})^2$, where $l_B = \sqrt{\frac{\hbar}{eB_z}}$ is the magnetic length, one finds for $B_z > 0$ that

$$\hat{q}_- = \frac{-i}{l_B}\sqrt{\frac{\rho}{2}}e^{-i\varphi}\left(1 + 2\partial_\rho - \frac{i}{\rho}\partial_\varphi\right) = \frac{-i\sqrt{2}}{l_B}\hat{\alpha}_-, \quad (8a)$$

$$\hat{q}_+ = \frac{i}{l_B}\sqrt{\frac{\rho}{2}}e^{i\varphi}\left(1 - 2\partial_\rho - \frac{i}{\rho}\partial_\varphi\right) = \frac{i\sqrt{2}}{l_B}\hat{\alpha}_+. \quad (8b)$$

The eigenfunctions of the operators $\hat{\alpha}_+$ and $\hat{\alpha}_-$, which are (i) regular at $\rho = 0$ and (ii) also eigenfunctions of $\hat{l}_z$, are $g_{a,l}(\rho,\varphi) = e^{il\varphi}\rho^{|l|/2}e^{-\rho/2}M(a,|l|+1,\rho)$, where l is an integer and $M(a,|l|+1,\rho)$ is the confluent hypergeometric function of the first kind [58]. One can show that

$$\hat{\alpha}_+\hat{\alpha}_- g_{a,l}(\rho,\varphi) = \begin{cases} -a g_{a,l}(\rho,\varphi) & \text{if } l \leq 0 \\ (l-a)g_{a,l}(\rho,\varphi) & \text{if } l > 0. \end{cases} \quad (9)$$

(For details, see Appendix C.) Considering now the Schrödinger equation for the bulk problem, i.e., for $V_{\mathrm{dot}} = 0$ in valley τ for spin s, it reads

$$\left[\hbar\omega_c^{\tau,s}\hat{\alpha}_+\hat{\alpha}_- + \frac{1}{2}\mathrm{sgn}(B_z)\hbar\omega_c^{\tau,s} + \tau\Delta_{\mathrm{CB}}s_z \right.$$
$$\left. + \left(\frac{\tau}{2}g_{\mathrm{vl}}\mu_{\mathrm{vl}} + \frac{1}{2}g_{\mathrm{sp}}^{\perp}\mu_B s_z\right)B_z\right]\Psi = E\Psi, \quad (10)$$

where $\Theta(x)$ is the Heaviside step function. The wave functions $\Psi_l^{\uparrow}(\rho,\varphi) = \frac{e^{il\varphi}}{\sqrt{2\pi}}\binom{1}{0}\Phi_l(\rho)$ and $\Psi_l^{\downarrow}(\rho,\varphi) = \frac{e^{il\varphi}}{\sqrt{2\pi}}\binom{0}{1}\Phi_l(\rho)$ will be eigenfunctions if $\Phi_l(\rho) = \rho^{|l|/2}e^{-\rho/2}M(a_l,|l|+1,\rho)$ and

$$\hbar\omega_c^{\tau,s}a_l = \begin{cases} E^{\tau,s} & \text{if } l \leq 0 \\ E^{\tau,s} + l\hbar\omega_c^{\tau,s} & \text{if } l > 0. \end{cases} \quad (11)$$

Here, $E^{\tau,s} = (1/2)\mathrm{sgn}(B_z)\hbar\omega_c^{\tau,s} + \tau s\Delta_{\mathrm{CB}} + \frac{1}{2}(\tau g_{\mathrm{vl}}\mu_{\mathrm{vl}} + s g_{\mathrm{sp}}^{\perp}\mu_B)B_z - E$. The bound state solutions of the QD problem are determined by the condition that the wave function has to vanish at $r = R_d$; i.e., one has to find the energy $E_l^{\tau,s}$ for which $M(a_l,|l|+1,\rho[r = R_d]) = 0$. The task is, therefore, to find, for a given magnetic field B_z and quantum number l, the roots of $M(a_l,|l|+1,\rho[r = R_d]) = 0$ as a function of a_l. The a_l values can be calculated numerically. Once the nth root $a_{n,l}$ is known, the energy of the bound state $E_{n,l}^{\tau,s}$ can be expressed using Eq. (11).

The numerically calculated spectrum for a QD with $R_d = 40$ nm in MoS$_2$ is shown in Fig. 4(a). At zero magnetic field, because of the quadratic dispersion in our model, there is an effective time-reversal symmetry acting within each valley and, therefore, states with angular momentum $\pm l$ within the same valley are degenerate. For finite magnetic field, all levels are both valley *and* spin split. For even larger magnetic fields, when $l_B \lesssim R_d$, the dot levels merge into Landau levels. Since Δ_{CB} is relatively small with respect to the cyclotron energy $\hbar\omega_c^{\tau,s}$, spin-split states $\downarrow$ and $\uparrow$ from the same valley can cross at some larger, but still finite, magnetic field [see, e.g., the crossing between the black and green lines for $E > 3$ meV for states in valley K in Fig. 4(a)].

Taking into account the Bychkov-Rashba SOC turns the crossings between states $|a,l,\uparrow\rangle$ and $|a,l+1,\downarrow\rangle, l \geq 0$ into avoided crossings. The selection rules for H_{BR}^{τ} can be derived by rewriting $\tilde{H}_{\mathrm{BR}}^{\tau}$ in terms of the operators α_- and α_+ and calculating their effect on the nonperturbed eigenstates (see Appendix C for details). For the low-lying energy states, in which we are primarily interested, the effect of the Bychkov-Rashba SOC is to introduce level repulsion between these states and higher energy ones allowed by the selection rules. Taking $|\lambda_{\mathrm{BR}}|/l_B$ as a characteristic energy

FIG. 5   Spectrum of a 40 nm WS$_2$ QD as a function of the perpendicular magnetic field $B_z > 0$. Black (red) lines show the spin $\uparrow$ ($\downarrow$) states from valley K (K'). The values of $m_{\text{eff}}^{\tau,s}$ can be found in Table I, whereas $g_{\text{vl}} = 1.6$ and $g_{\text{sp}}^{\perp} = 1.99$ (see Table 2).
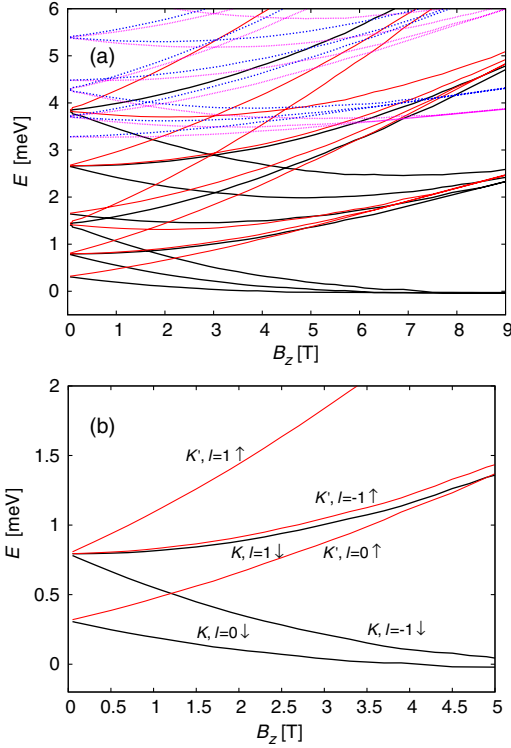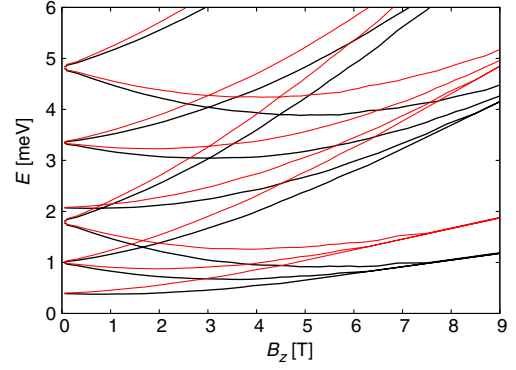
FIG. 4   (a) Spectrum of a MoS$_2$ QD of radius $R_d = 40$ nm as a function of the perpendicular magnetic field $B_z > 0$. Black (purple) lines: spin $\downarrow$ ($\uparrow$) in the K valley; red (blue) lines: spin $\uparrow$ ($\downarrow$) in the K' valley. States up to $|l| = 2$ and $n = 2$ are shown. (b) Part of the spectrum shown in (a) for small magnetic fields and low energies. Labels show the valley, orbital quantum number l, and spin state for each level. The values of $m_{\text{eff}}^{\tau,s}$, g_{vl}, and $g_{\text{sp}}^{\perp}$ used in the calculations can be found in Tables I and II.

different valleys is significantly larger for the former material than for the latter [compare Figs. 4(b) and 5]. This is due to the different sign of Δ_{CB} and, hence, different spin polarization of the lowest levels in the two materials: in the case of MoS$_2$, the valley splitting (described by H_{vl}^{τ}) and the coupling of the spin to the magnetic field (given by $H_{\text{sp,tot}}$) reinforce each other, whereas for WS$_2$, they counteract, and since g_{vl} and $g_{\text{sp}}^{\perp}$ have similar magnitude, in the end the valley splitting of the levels at large magnetic fields is small. This suggests that for spin and valley filtering the MoX$_2$ compounds are better suited.

The qualitative difference between MoS$_2$ and WS$_2$ regarding the valley splitting does not depend crucially on the exact values of the bulk parameters $\tilde{g}_{\text{vl}}$ and $g_{\text{so}}^{\perp}$. However, on a more quantitative level, the valley splitting does depend on the exact values of the valley and spin g factors, which were calculated using the DFT band gap and the $\mathbf{k} \cdot \mathbf{p}$ parameter γ_3 (see Appendix B for details). It is known that DFT underestimates the band gap, and the value of γ_3 depends to some extent on the way it is extracted from

scale of this coupling and using Table III, one can see that for magnetic fields $\lesssim 10$ T and electric fields $E_z \lesssim 10^{-2}$ V/Å the level repulsion is much smaller than the spin splitting Δ_{CB} and, therefore, we neglect it.

Figure 4(b) shows the low-field and low-energy regime of Fig. 4(a). As one can see, for $B_z \gtrsim 1$ T the lowest energy states reside in valley K. We emphasize that, in contrast to gapped monolayer [38,59,60] and bilayer [38,60] graphene, the energy states are also spin polarized. This suggests that QDs in MoS$_2$ can be used as simultaneous valley and spin filters.

Figure 5 shows the low-energy spectrum of a WS$_2$ QD with radius $R_d = 40$ nm. Qualitatively, it is similar to MoS$_2$, but because the spin splitting Δ_{CB} between the $\uparrow$ and $\downarrow$ states belonging to the same valley is much larger than was the case for MoS$_2$, they do not cross for the magnetic field range shown in Fig 5. One can also observe that the $B_z = 0$ level spacing is somewhat larger than in the MoS$_2$ QD [see Fig. 4(b)]. Another important observation that can be made by comparing the results for MoS$_2$ and WS$_2$ is the following: for a given magnetic field, e.g., $B_z = 5$ T, the splitting between states belonging to
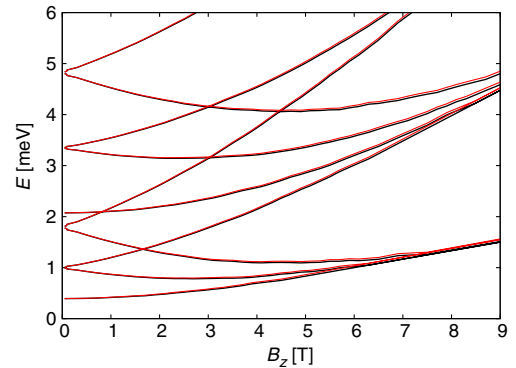

FIG. 6   Spectrum of a 40 nm WS$_2$ QD as a function of the perpendicular magnetic field $B_z > 0$. The values of $m_{\text{eff}}^{\tau,s}$ can be found in Table I and we used $g_{\text{vl}} = 2.31$ and $g_{\text{sp}}^{\perp} = 1.84$ (cf. Fig. 5). Black (red) lines show spin $\uparrow$ ($\downarrow$) states from the K (K') valley.

the FP computations. As a result, the values shown in Table II probably overestimate $\tilde{g}_{\text{vl}}$ and $g_{\text{so}}^{\perp}$. To illustrate this point, in Fig. 6 we show the low-energy spectrum of the same WS$_2$ quantum dot as in Fig. 5 but using a g_{vl} ($g_{\text{sp}}^{\perp}$), which was obtained from a $\tilde{g}_{\text{vl}}$ ($g_{\text{so}}^{\perp}$) that is $\sim$20% smaller than the one shown in Table II. The valley splitting of the bound states can now barely be observed.

B. Qubits in TMDC quantum dots

Circular hard-wall QDs in two-dimensional semiconducting TMDCs have a spectrum similar to the characteristic Fock-Darwin spectrum for harmonically confined QDs (Fig. 4). Taking MoS$_2$ as an example, due to the intrinsic spin-orbit splitting of about 3 meV, each of the spin- and valley-degenerate states $|l\rangle$ splits into two Kramers pairs at vanishing magnetic field $B = 0$, namely, ($|l, K, \uparrow\rangle$, $|l, K', \downarrow\rangle$) and ($|l, K', \uparrow\rangle$, $|l, K, \downarrow\rangle$). Only at relatively high magnetic fields do we observe a crossing of two states with the same spin and opposite valley or within the same valley with opposite spin. These valley and spin pairs could serve as valley or spin qubits, respectively, but the required high magnetic field and the other overlapping levels with different l' quantum numbers complicate their realization. (The energy of higher angular momentum states can, in principle, be increased by making the QD smaller.)

In view of the above, the most realistic approach seems to be to use the lowest Kramers pairs around $B = 0$, e.g., $|l = 0, K', \uparrow\rangle$ and $|l = 0, K, \downarrow\rangle$, as a combined spin-valley qubit [54,61]. The energy splitting of these two-level systems could be tuned using the external magnetic field. The relaxation time of such spin-valley qubits in TMDC QDs will be limited only by the longer spin or valley relaxation time, while the pure dephasing time will be limited by the shorter of the two. The exchange interaction then provides the necessary coupling of adjacent spin-valley qubits for the realization of two-qubit gates.

IV. SUMMARY

In summary, we study TMDCs as possible host materials for QDs and qubits. We consider n-doped samples, which can be described by an effective model that involves only the CB. Using our FP calculations, we obtain the parameters that appear in the effective Hamiltonian (effective masses, g factors) for four distinct TMDC materials. We discuss the effects of external magnetic and electric fields, pointing out that the former leads to the splitting of the energy levels in different valleys, while the latter induces a Bychkov-Rashba SOC, which, however, appears to be rather small. We use the effective Hamiltonian to calculate the spectrum of circular QDs, finding that all bound states are both spin and valley split. Our results suggest that, at large magnetic field, QDs in TMDCs can be used as spin and valley filters, but that this effect may depend on

material-specific details. Finally, we discuss the possible types of qubits that QDs in TMDC materials can host. We find that Kramers pairs around $B_z = 0$ appear to be the most realistic candidates.

The effective one-band model and the material parameters that we obtain for different TMDCs will hopefully be helpful in other fields as well, e.g., for studying plasmonic excitations [62].

ACKNOWLEDGMENTS

Note added.—Recently, another article on the spin splitting in the conduction band of monolayer TMDCs was published (Ref. [63]).

APPENDIX A: SEVEN-BAND MODEL

1. Introduction

Our aim is to derive a low-energy effective Hamiltonian valid close to the K (K') point of the BZ, which describes the band dispersion, the effects of intrinsic SOC, and the SOC induced by an external electric field (Bychkov-Rashba effect). To this end, we consider the SOC in the atomic approximation, apply $\mathbf{k} \cdot \mathbf{p}$ perturbation theory, and take into account the effect of an external electric field perturbatively. We consider a seven-band model (without spin) that contains every band from the third band below the VB (which we call VB-3) up to the second band above the CB (denoted by CB + 2); i.e., we take the basis $\{|\Psi_{E_2'}^{\text{VB}-3}, s\rangle, |\Psi_{E_1'}^{\text{VB}-2}, s\rangle, |\Psi_{E_2'}^{\text{VB}-1}, s\rangle, |\Psi_{A'}^{\text{VB}}, s\rangle, |\Psi_{E_1'}^{\text{CB}}, s\rangle, |\Psi_{A'}^{\text{CB}+1}, s\rangle, |\Psi_{E_1'}^{\text{CB}+2}, s\rangle\}$. The upper index $b = \{\text{VB} - 3, \text{VB} - 2, \text{VB} - 1, \text{VB}, \text{CB}, \text{CB} + 1, \text{CB} + 2\}$ denotes the band, and the lower index μ indicates the pertinent irreducible representation of the point group C_{3h}, which is the pertinent symmetry group for the unperturbed basis functions at the K point of the BZ. The spinful symmetry basis functions are represented by $|\Psi_\mu^b, s\rangle = |\Psi_\mu^b\rangle \otimes |s\rangle$, where $s = \{\uparrow, \downarrow\}$ denotes the spin degree of freedom. Note that the basis states can be separated into two groups. The first group contains those states whose orbital part is symmetric with respect to the mirror operation σ_h: $\{|\Psi_{A'}^{\text{VB}}, s\rangle, |\Psi_{E_1'}^{\text{CB}}, s\rangle, |\Psi_{E_2'}^{\text{VB}-3}, s\rangle, |\Psi_{E_1'}^{\text{CB}+2}, s\rangle\}$; the second group contains antisymmetric states: $\{|\Psi_{E_1'}^{\text{VB}-2}, s\rangle, |\Psi_{E_2'}^{\text{VB}-1}, s\rangle, |\Psi_{A'}^{\text{CB}+1}, s\rangle\}$.

2. Intrinsic spin-orbit coupling at the K (K') point of the Brillouin zone

The intrinsic SOC is treated in the atomic approximation, whereby the SOC is given by the Hamiltonian [43]

TABLE IV.　SOC matrix of TMDCs at the K point in the seven-band model.

H_{so}^K	$\|\Psi_{A'}^{VB}, s\rangle$	$\|\Psi_{E_1'}^{CB}, s\rangle$	$\|\Psi_{E_2'}^{VB-3}, s\rangle$	$\|\Psi_{E_2'}^{CB+2}, s\rangle$	$\|\Psi_{E_1'}^{VB-2}, s\rangle$	$\|\Psi_{E_2'}^{VB-1}, s\rangle$	$\|\Psi_{A'}^{CB+1}, s\rangle$
$\|\Psi_{A'}^{VB}, s\rangle$	$s_z\Delta_v$	0	0	0	$s_-\Delta_{v,v-2}$	$s_+\Delta_{v,v-2}$	0
$\|\Psi_{E_1'}^{CB}, s\rangle$	0	$s_z\Delta_c$	0	0	0	$s_-\Delta_{c,v-1}$	$s_+\Delta_{c,c+1}$
$\|\Psi_{E_2'}^{VB-3}, s\rangle$	0	0	$s_z\Delta_{v-3}$	$s_z\Delta_{v-3,c+2}$	$s_+\Delta_{v-3,v-2}$	0	$s_-\Delta_{v-3,c+1}$
$\|\Psi_{E_2'}^{CB+2}, s\rangle$	0	0	$s_z\Delta_{v-3,c+2}^*$	$s_z\Delta_{c+2}$	$s_+\Delta_{c+2,v-2}$	0	$s_-\Delta_{c+2,c+1}$
$\|\Psi_{E_1'}^{VB-2}, s\rangle$	$s_+\Delta_{v,v-2}^*$	0	$s_-\Delta_{v-3,v-2}^*$	$s_-\Delta_{c+2,v-2}^*$	$s_z\Delta_{v-2}$	0	0
$\|\Psi_{E_2'}^{VB-1}, s\rangle$	$s_-\Delta_{v,v-1}^*$	$s_+\Delta_{c,v-1}^*$	0	0	0	$s_z\Delta_{v-1}$	0
$\|\Psi_{A'}^{CB+1}, s\rangle$	0	$s_-\Delta_{c,c+1}^*$	$s_+\Delta_{v-3,c+1}^*$	$s_+\Delta_{c+2,c+1}^*$	0	0	$s_z\Delta_{c+1}$

$$\mathcal{H}_{so}^{at} = \frac{\hbar}{4m_e^2 c^2}\frac{1}{r}\frac{dV(r)}{dr}\hat{\mathbf{L}}\cdot\hat{\mathbf{S}}. \tag{A1}$$

Here, $V(r)$ is the spherically symmetric atomic potential, $\hat{\mathbf{L}}$ is the angular momentum operator, and $\hat{\mathbf{S}} = (s_x, s_y, s_z)$ is a vector of spin Pauli matrices s_x, s_y, s_z (with eigenvalues ± 1). One can rewrite the product $\hat{\mathbf{L}}\cdot\hat{\mathbf{S}}$ as $\hat{\mathbf{L}}\cdot\hat{\mathbf{S}} = \hat{L}_z s_z + \hat{L}_+ s_- + \hat{L}_- s_+$, where $\hat{L}_\pm = \hat{L}_x \pm i\hat{L}_y$ and $s_\pm = \frac{1}{2}(s_x \pm is_y)$. The task is then to calculate the matrix elements of Eq. (A1) in the basis introduced in Appendix A1 at the K (K') point of the BZ. To this end, one can make use of the symmetries of the band-edge wave functions. For instance, the diagonal matrix elements are proportional to s_z. This is because the $\hat{L}_z$ is symmetric with respect to σ_h, whereas $\hat{L}_\pm$ is antisymmetric. Conversely, most of the off-diagonal matrix elements will be proportional to $s_\pm$, reflecting the fact that they are related to matrix elements having different symmetry with respect to σ_h. The only exception is the off-diagonal matrix element between $|\Psi_{E_2'}^{v-3}, s\rangle$ and $|\Psi_{E_1'}^{c+2}, s\rangle$, which connects symmetric states. In addition, one has to consider the transformation properties of the basis functions and angular momentum operators with respect to a rotation by $2\pi/3$. The general result for the K point is shown in Table IV.

Before showing further details of the calculations in Appendixes A 3 and A 4, some comments are in order. As long as one considers states close to the K point, the largest energy scale is the band gap and other band-edge energy differences. The next largest energy scale comes from the SOC. As an upper limit of the various diagonal and off-diagonal matrix elements (see Table IV) one can take the spin splitting of the VB. The reason is that the main contribution to this band at the K point comes from the metal d orbitals, and the metal atoms, being much heavier than the chalcogenides, are expected to dominate the SOC (with the possible exception of the CB). This is smaller than the typical interband energies for the MoX$_2$ materials, and, therefore, the different bands are only weakly hybridized by the SOC. For the heavier WX$_2$ compounds, the VB spin splitting is 425–460 meV, indicating that some matrix elements may not be small any more with respect to band-

edge energy differences. One is, therefore, tempted to first perform a diagonalization of the SOC Hamiltonian (see Table IV) to obtain the eigenstates $|\Psi_{\mu,\mu'}^b, s\rangle$, which will be some linear combination of the original basis states $|\Psi_\mu^b, s\rangle$, and then perform the $\mathbf{k}\cdot\mathbf{p}$ expansion and the perturbation calculation for the external electric field using this new basis. Diagonalization of the Hamiltonian (Table IV) is possible if one neglects the matrix elements $\Delta_{v-3,c+1}$, $\Delta_{v-3,c+2}$, and $\Delta_{v-2,c+2}$ between remote bands. The eigenstates are linear combinations of a symmetric and an antisymmetric basis vector. However, the subsequent calculations in Appendixes A 3 and A 4, as well as the final Löwdin partitioning, are more tractable if we do not make this diagonalization and stay with the original basis states throughout the calculations. The two approaches give the same results in the leading order of the ratio of the various SOC matrix elements and band-edge energy differences. For MoX$_2$ compounds, the approach outlined below is adequate: for the heavier WX$_2$ materials, it still gives reasonable results, but the numerical estimates for, e.g., the effective g factor might have to be revised, once experimental and theoretical consensus is reached regarding the magnitude of the band gap and SOC band splittings.

The SOC Hamiltonian at K' can be obtained by making the following substitutions: $\Delta_b \to \Delta_b^*$, $\Delta_{b,b'} \to \Delta_{b,b'}^*$, $s_\pm \to -s_\mp$, $s_z \to -s_z$. These relations follow from the fact that the orbital wave functions at K and K' are connected by time-reversal symmetry; i.e., $|\Psi_\mu^b(K)\rangle = \hat{K}_0|\Psi_{\mu'}^b(K')\rangle$, where $\hat{K}_0$ denotes complex conjugation. Consider, as an example, a matrix element $\langle\Psi_\mu^b(K')|\hat{L}_z|\Psi_{\mu'}^{b'}(K')\rangle$:

$$\langle\Psi_\mu^b(K')|\hat{L}_z|\Psi_{\mu'}^{b'}(K')\rangle = \langle\hat{K}_0\Psi_\nu^b(K)|\hat{L}_z|\hat{K}_0\Psi_{\nu'}^{b'}(K)\rangle$$
$$= \langle\hat{K}_0\Psi_\nu^b(K)|\hat{L}_z\hat{K}_0\Psi_{\nu'}^{b'}(K)\rangle$$
$$= \langle\hat{K}_0\Psi_\nu^b(K)|(-1)\hat{K}_0[\hat{L}_z\Psi_{\nu'}^{b'}(K)]\rangle$$
$$= -\langle[\hat{L}_z\Psi_{\nu'}^{b'}(K)]|\Psi_\nu^b(K)\rangle$$
$$= -(\langle\Psi_\nu^b(K)|\hat{L}_z\Psi_{\nu'}^{b'}(K)\rangle)^*.$$

Here, we have made use of $\hat{K}_0\hat{L}_z = -\hat{L}_z\hat{K}_0$. Relations for the matrix elements involving the operators $\hat{L}_\pm$ can be

obtained by noting that $\hat{K}_0 \hat{L}_\pm = -\hat{L}_\mp \hat{K}_0$ and, therefore, $\langle \Psi_\mu^b(K') | \hat{L}_\pm | \Psi_{\mu'}^{b'}(K') \rangle = -(\langle \Psi_\nu^b(K) | \hat{L}_\mp | \Psi_{\nu'}^{b'}(K) \rangle)^*$.

3. k · p matrix elements at the K (K′) points

The Hamiltonian $\mathcal{H}_{\mathbf{k} \cdot \mathbf{p}} = \frac{1}{2} \frac{\hbar}{m_e} (q_+ \hat{p}_- + q_- \hat{p}_+)$ has non-zero matrix elements only between states $|\Psi_\mu^b, s\rangle$ and $|\Psi_{\mu'}^{b'}, s\rangle$, which are both either symmetric or antisymmetric with respect to the mirror operation σ_h. For the discussion in the main text, we need only the matrix elements between symmetric states. These matrix elements, which are diagonal in the spin space, have already been obtained in Ref. [26], but for convenience they are replicated in Table V. We note that, in addition to $\hat{p}_\pm$, another operator due to SOC appears in the calculation of the $\mathbf{k} \cdot \mathbf{p}$ matrix elements [43,64], but it can be neglected. The diagonal elements in Table V are the band-edge energies.

The matrix elements at the K' point can be obtained with the substitutions $\gamma_i \to \gamma_i^*$ and $q_\pm \to -q_\mp$. This follows from

$$\begin{aligned}
\langle \Psi_\mu^b(K') | \mathcal{H}_{\mathbf{k} \cdot \mathbf{p}} | \Psi_{\mu'}^{b'}(K') \rangle &= \langle \hat{K}_0 \Psi_\nu^b(K) | \mathcal{H}_{\mathbf{k} \cdot \mathbf{p}} | \hat{K}_0 \Psi_{\nu'}^{b'}(K) \rangle \\
&= \langle \hat{K}_0 \Psi_\nu^b(K) | (-1) \hat{K}_0 [\mathcal{H}_{\mathbf{k} \cdot \mathbf{p}} \Psi_{\nu'}^{b'}(K)] \rangle \\
&= -\langle \mathcal{H}_{\mathbf{k} \cdot \mathbf{p}} \Psi_{\nu'}^{b'}(K)] | \Psi_\nu^b(K) \rangle \\
&= -(\langle \Psi_\nu^b(K) | \mathcal{H}_{\mathbf{k} \cdot \mathbf{p}} \Psi_{\nu'}^{b'}(K) \rangle)^*.
\end{aligned}$$

As mentioned in Ref. [26], concrete values for the γ_i parameters can be obtained from either fitting the band dispersion or using the Kohn-Sham orbitals to directly evaluate the matrix elements $\langle \Psi_\mu^b | \hat{p}_\pm | \Psi_{\mu'}^{b'} \rangle$. The latter can be done, e.g., with the help of the CASTEP code (see Appendix D for computational details). To estimate the effective valley and spin g factor (Appendix B1) and the Bychkov-Rashba SOC parameter (Appendix B4), we need the value of γ_3, for which the two approaches give similar results.

External magnetic field.—The effects of an external magnetic field in the $\mathbf{k} \cdot \mathbf{p}$ formalism can be obtained by using the Kohn-Luttinger prescription [43], which amounts to replacing the numbers q_x, q_y in the above formulas with the operators $\hat{\mathbf{q}} = \frac{1}{i} \nabla + \frac{e}{\hbar} \mathbf{A}$, where $\mathbf{A}$ is the vector potential and $e > 0$ is the magnitude of the electron charge. Note

that, due to this replacement, $\hat{q}_+$ and $\hat{q}_-$ become non-commuting operators and their order has to be preserved when one folds down the above multiband Hamiltonian to obtain a low-energy effective Hamiltonian. Using the Landau gauge to describe a homogeneous, perpendicular magnetic field, the commutation relation is $[\hat{q}_-, \hat{q}_+] = \frac{2eB_z}{\hbar}$.

4. External electric field

In order to derive the Bychkov-Rashba SOC, we assume that a homogeneous, perpendicular external electric field is present, which can be described by the Hamiltonian $U(z) = eE_z z$. It breaks the mirror symmetry σ_h and, therefore, couples symmetric and antisymmetric basis states, while the matrix elements between states of the same symmetry are zero. The full symmetry at the K point is lowered from C_{3h} to C_3; i.e., the threefold rotational symmetry is not broken. The matrix elements of H_U^K between the symmetric and antisymmetric states are shown in Table VI.

The matrix elements $\xi_{b,b'} = eE_z \langle \Psi_\mu^b | z | \Psi_{\mu'}^{b'} \rangle = eE_z \zeta_{b,b'}$ are in general complex numbers. The magnitude of $\zeta_{b,b}$ can be calculated using the band-edge Kohn-Sham orbitals, as in Ref. [47], where this approach was used to estimate the electric field–induced band gap in silicene (see Appendix D for computational details). Since the Kohn-Sham orbitals are defined only up to an arbitrary phase, we cannot extract the real and imaginary parts of $\zeta_{b,b'}$ from the actual calculation. The matrix elements at the K' point can be obtained by complex conjugation of the K-point matrix elements.

APPENDIX B: EFFECTIVE LOW-ENERGY HAMILTONIAN FOR THE CONDUCTION BAND

The total Hamiltonian of the system is then given by

$$\tilde{H} = \tilde{H}_{\mathbf{k} \cdot \mathbf{p}} + \tilde{H}_{\mathrm{so}} + \tilde{H}_U. \tag{B1}$$

Because our seven-band model contains bands that are far from the CB, our next step is to derive an effective Hamiltonian for the spin-split CB. This can be done by systematically eliminating all other bands using Löwdin partitioning [64]. Because the trigonal warping in the CB is weak, we consider terms up to second order in $\mathbf{q}$. We also

TABLE VI. Matrix elements of the external electric field at the K point between symmetric and antisymmetric states.

H_U^K	$|\Psi_{E_1'}^{\mathrm{VB}-2}, s\rangle$	$|\Psi_{E_2'}^{\mathrm{VB}-1}, s\rangle$	$|\Psi_{A'}^{\mathrm{CB}+1}, s\rangle$
$|\Psi_{A'}^{\mathrm{VB}}, s\rangle$	0	0	$\xi_{v,c+1}$
$|\Psi_{E_1'}^{\mathrm{CB}}, s\rangle$	$\xi_{c,v-2}$	0	0
$|\Psi_{E_2'}^{\mathrm{VB}-3}, s\rangle$	0	$\xi_{v-3,v-1}$	0
$|\Psi_{E_2'}^{\mathrm{CB}+2}, s\rangle$	0	$\xi_{c+2,v-1}$	0

TABLE V. The $\mathbf{k} \cdot \mathbf{p}$ matrix elements between symmetric states at the K point.

$H_{\mathbf{k} \cdot \mathbf{p}}^K$	$|\Psi_{A'}^{\mathrm{VB}}, s\rangle$	$|\Psi_{E_1'}^{\mathrm{CB}}, s\rangle$	$|\Psi_{E_2'}^{\mathrm{VB}-3}, s\rangle$	$|\Psi_{E_2'}^{\mathrm{CB}+2}, s\rangle$
$|\Psi_{A'}^{\mathrm{VB}}, s\rangle$	ε_v	$\gamma_3 q_-$	$\gamma_2 q_+$	$\gamma_4 q_+$
$|\Psi_{E_1'}^{\mathrm{CB}}, s\rangle$	$\gamma_3^* q_+$	ε_c	$\gamma_5 q_-$	$\gamma_6 q_-$
$|\Psi_{E_2'}^{\mathrm{VB}-3}, s\rangle$	$\gamma_2^* q_-$	$\gamma_5^* q_+$	ε_{v-3}	0
$|\Psi_{E_2'}^{\mathrm{CB}+2}, s\rangle$	$\gamma_4^* q_-$	$\gamma_6^* q_+$	0	ε_{c+2}

keep the lowest nonvanishing order in the product of $\hat{q}_{\pm}$ and the SOC and electric field matrix elements.

At the K point, one finds that the effective Hamiltonian is given by

$$\tilde{H}_{\text{el}}^{K,s} = \frac{\hbar^2 \hat{q}^2}{2m_e} + \frac{|\gamma_3|^2}{\varepsilon_c^{K,s} - \varepsilon_v^{K,s}} \hat{q}_+ \hat{q}_- + \left[\frac{|\gamma_5|^2}{\varepsilon_c^{K,s} - \varepsilon_{v-3}^{K,s}} + \frac{|\gamma_6|^2}{\varepsilon_c^{K,s} - \varepsilon_{c+2}^{K,s}} \right] \hat{q}_- \hat{q}_+, \quad \text{(B2a)}$$

$$\tilde{H}_{\text{so,intr}}^{K,s} = s\Delta_c^K + \frac{|\Delta_{c,c+1}|^2}{\varepsilon_c^{K,\uparrow} - \varepsilon_{c+1}^{K,\downarrow}} s_+ s_- + \frac{|\Delta_{c,v-1}|^2}{\varepsilon_c^{K,\downarrow} - \varepsilon_{v-1}^{K,\uparrow}} s_- s_+ \quad \text{(B2b)}$$

$$\tilde{H}_U^{K,s} = \frac{|\xi_{c,v-2}|^2}{\varepsilon_c^{K,s} - \varepsilon_{v-2}^{K,s}}, \quad \text{(B2c)}$$

$$\tilde{H}_{\text{BR}}^K = \begin{pmatrix} 0 & \lambda_{\text{BR}}^* \hat{q}_- \\ \lambda_{\text{BR}} \hat{q}_+ & 0 \end{pmatrix}, \quad \text{(B2d)}$$

whereas at the K' point,

$$\tilde{H}_{\text{el}}^{K',s} = \frac{\hbar^2 \hat{q}^2}{2m_e} + \frac{|\gamma_3|^2}{\varepsilon_c^{K',s} - \varepsilon_v^{K',s}} \hat{q}_- \hat{q}_+ + \left[\frac{|\gamma_5|^2}{\varepsilon_c^{K',s} - \varepsilon_{v-3}^{K',s}} + \frac{|\gamma_6|^2}{\varepsilon_c^{K',s} - \varepsilon_{c+2}^{K',s}} \right] \hat{q}_+ \hat{q}_-, \quad \text{(B3a)}$$

$$\tilde{H}_{\text{so,intr}}^{K',s} = s\Delta_c^{K'} + \frac{|\Delta_{c,c+1}|^2}{\varepsilon_c^{K',\downarrow} - \varepsilon_{c+1}^{K',\uparrow}} s_- s_+ + \frac{|\Delta_{c,v-1}|^2}{\varepsilon_c^{K',\uparrow} - \varepsilon_{v-1}^{K',\downarrow}} s_+ s_- \quad \text{(B3b)}$$

$$\tilde{H}_U^{K',s} = \frac{|\xi_{c,v-2}|^2}{\varepsilon_c^{K',s} - \varepsilon_{v-2}^{K',s}}, \quad \text{(B3c)}$$

$$\tilde{H}_{\text{BR}}^{K'} = \begin{pmatrix} 0 & \lambda_{\text{BR}}^* \hat{q}_- \\ \lambda_{\text{BR}} \hat{q}_+ & 0 \end{pmatrix}. \quad \text{(B3d)}$$

In the above formulas, m_e is the bare electron mass and we use the notation $\varepsilon_b^{K(K'),s} = \varepsilon_b + s\Delta_b^{K,(K')}$, where $s = \pm 1$ is the spin quantum number, $\Delta_b^{K,(K')}$ are the diagonal SOC matrix elements from Appendix A2 at the K, (K') point, and ε_b are the band-edge energies defined in Appendix A3, i.e., not taking into account the SOC. For convenience, we introduced the shorthand notation $\uparrow$ for $s = 1$ and $\downarrow$ for $s = -1$ in Eqs. (B2b) and (B3b). Making use of the fact that the K and K' valleys are connected by time-reversal

symmetry (see Appendix A2), we write $\Delta_b^{K,(K')} = \tau \Delta_b$, where $\tau = 1$ (-1) for K (K'), and we can introduce the notation $\varepsilon_b^{\tau,s} = \varepsilon_b + \tau s \Delta_b$.

The first term in Eqs. (B2a) and (B3a) is the free-electron contribution [43,64]. Regarding the other terms in Eqs. (B2a) and (B3a) that contain $\hat{q}_+$ and $\hat{q}_-$, we do not assume that they commute; see Appendix B1. Note that $\tilde{H}_{\text{el}}$, $\tilde{H}_{\text{so,intr}}$, and $\tilde{H}_U$ are diagonal in spin space, but the Bychkov-Rashba Hamiltonian $\tilde{H}_{\text{BR}}$ introduces coupling between $\uparrow$ and $\downarrow$. Now, we briefly discuss each of the terms appearing in Eqs. (B2) and (B3).

1. Electronic effective Hamiltonian H_{el}

In the electronic Hamiltonian H_{el}, we took into account the fact that, in the presence of an external magnetic field, the operators $\hat{q}_+$ and $\hat{q}_-$ do not commute. To obtain Eq. (1), one has to use the commutation relation $[\hat{q}_-, \hat{q}_+] = \frac{2eB_z}{\hbar}$ and rewrite $\frac{\hbar^2 \hat{q}^2}{2m_e}$ as $\frac{\hbar^2 \hat{q}_+ \hat{q}_-}{2m_e} + \frac{\hbar e B_z}{2m_e}$. One finds

$$\tilde{H}_{\text{el}}^{K,s} = \frac{\hbar^2 \hat{q}_+ \hat{q}_-}{2m_{\text{eff}}^{\tau=1,s}} + \frac{\hbar e B_z}{m_{\text{eff}}^{\tau=1,s}} - \left(\frac{1}{2m_e} + \frac{2|\tilde{\gamma}_3|^2}{\varepsilon_c^{\tau=1,s} - \varepsilon_v^{\tau=1,s}} \right) \hbar e B_z \quad \text{(B4)}$$

in the K valley and

$$\tilde{H}_{\text{el}}^{K',s} = \frac{\hbar^2 \hat{q}_+ \hat{q}_-}{2m_{\text{eff}}^{\tau=-1,s}} + \left(\frac{1}{2m_e} + \frac{2|\tilde{\gamma}_3|^2}{\varepsilon_c^{\tau=-1,s} - \varepsilon_v^{\tau=-1,s}} \right) \hbar e B_z \quad \text{(B5)}$$

in the K' valley. The effective mass $m_{\text{eff}}^{\tau,s}$ is given by

$$\frac{1}{2m_{\text{eff}}^{\tau,s}} = \frac{1}{2m_e} + \frac{|\tilde{\gamma}_3|^2}{\varepsilon_c^{\tau,s} - \varepsilon_v^{\tau,s}} + \frac{|\tilde{\gamma}_5|^2}{\varepsilon_c^{\tau,s} - \varepsilon_{v-3}^{\tau,s}} + \frac{|\tilde{\gamma}_6|^2}{\varepsilon_c^{\tau,s} - \varepsilon_{c+2}^{\tau,s}}. \quad \text{(B6)}$$

In the above formulas, $\tilde{\gamma}_i = \gamma_i/\hbar$. The inverse of the effective mass $m_{\text{eff}}^{\tau,s}$ can be then rewritten in terms of m_{eff}^0 and δm_{eff}, as shown below Eq. (1).

The difference δm_{eff} in the effective masses comes mainly from the spin splitting Δ_v and Δ_{c+2} of the VB and CB + 2, respectively, with other diagonal SOC matrix elements being much smaller. We attribute the heavier effective mass at the K point to the $\uparrow$ band. This assignment is based on the following. (i) From DFT calculations, we know that both the VB and the CB + 2 are mainly composed of $d_{x^2-y^2}$ and d_{xy} orbitals. Using group theoretical considerations, we take a VB Bloch wave function $\sim d_{x^2-y^2} - id_{xy}$, whereas in the case of the CB + 2, the Bloch wave function is $\sim d_{x^2-y^2} + id_{xy}$. (ii) Taking into account (i), we assume that $\Delta_v = \langle \Psi_{A'}^{\text{vb}}(K) | H_{\text{so}}^{\text{at}} | \Psi_{A'}^{\text{vb}}(K) \rangle < 0$

and $\Delta_{c+2} = \langle \Psi_{E_1'}^{vb+2}(K) | H_{so}^{at} | \Psi_{E_1'}^{cb+2}(K) \rangle > 0$. Regarding (i), we note that, since the states at the K point are related to the states at K' by time reversal, our choice for the VB Bloch wave function is equivalent to other choices in the literature [5,27] up to a possible relabeling of the valleys $K \leftrightarrow K'$. The sign of Δ_v, as shown below, affects the sign of the effective spin g factor; therefore, it should be possible to deduce it experimentally. (From symmetry considerations [25,26] and FP results [27], we also know that there is a small X-p orbital contribution to the VB and CB + 2 as well, but in contrast to the CB, which is discussed in Appendix B 2, this can be neglected in the case of the VB and CB + 2 spin splitting.)

The physical meaning of the term $[2|\tilde{\gamma}_3|^2/(\varepsilon_c^{\tau,s} - \varepsilon_v^{\tau,s})]\hbar e B_z$ appearing in Eqs. (B4) and (B5) is probably more transparent if one expands it in powers of $(\Delta_c - \Delta_v)/(\varepsilon_c - \varepsilon_v)$, where $E_{bg} = \varepsilon_c - \varepsilon_v$ is the band gap in the absence of SOC. The zeroth-order term yields the valley-splitting Hamiltonian $\tilde{H}_{vl}^\tau = -\tau \tilde{g}_{vl} \mu_B B_z$, with

$$\tilde{g}_{vl} = 1 + 4m_e |\tilde{\gamma}_3|^2 / E_{bg}. \tag{B7}$$

The higher-order terms in the expansion determine how the coupling of the spin to the magnetic field is modified due to the strong SOC in TMDCs. Keeping the first-order term only, one arrives at the Hamiltonian $\tilde{H}_{sp}^s = \frac{1}{2} g_{so}^\perp \mu_B B_z$, where g_{so} is an out-of-plane effective spin g factor,

$$g_{so}^\perp \approx 8m_e |\tilde{\gamma}_3|^2 \frac{\Delta_c - \Delta_v}{(E_{bg})^2}, \tag{B8}$$

where m_e is the bare electron mass. The value of Δ_c, i.e., the spin splitting coming from the X-p orbitals in the CB (see Appendix B 2), is not known; however, we can safely assume that it is negligible with respect to Δ_v. As explained above, we assume that $\Delta_v < 0$, so we find that $g_{so}^\perp \approx 8m_e |\tilde{\gamma}_3|^2 |\Delta_v|/(E_{bg}^2)$. We note that in the case of bulk semiconductors, a similar formula to Eq. (B8) is called Roth's formula [65].

The relevant parameters Δ_v, $|\gamma_3|$, and E_{bg} to calculate g_{vl} and $g_{so}^\perp$ are shown in Table VII.

The parameter γ_3 was obtained with the help of Kohn-Sham orbitals (see Appendix A 3), while the band gap $E_{bg} = \varepsilon_c - \varepsilon_v$ is readily available from our DFT calculations. We note that, because E_{bg} is underestimated in DFT,

the values of g_{vl} and g_{so} shown in Table II are overestimated.

2. Intrinsic SOC Hamiltonian $H_{so,int}$

Starting from Eqs. (B2b) and (B3b), it is easy to show that, apart from a constant term, the intrinsic SOC Hamiltonian $H_{so,int}$ can be written as shown in Eq. (1), with $\Delta_{CB} = \Delta_c + (\omega_1 - \omega_2)/2$, where $\omega_1 \approx |\Delta_{c,c+1}|^2/(\varepsilon_c - \varepsilon_{c+1})$ and $\omega_2 \approx |\Delta_{c,v-1}|^2/(\varepsilon_c - \varepsilon_{v-1})$ and in the denominators we use $\varepsilon_b^{\tau,s} \approx \varepsilon_b$.

The spin splitting in the CB is discussed in Refs. [26,36,45]. Using our latest FP results, we revisit and expand our previous discussion [26] of the problem. Generally, the intrinsic SOC Hamiltonian $H_{so,int}$ has two contributions. One contribution comes from the coupling of the CB to other, remote bands and is, therefore, second order in the off-diagonal SOC matrix elements. In our seven-band model, the couplings to VB − 1 and CB + 1, described by $\Delta_{c,c+1}$ and $\Delta_{c,v-1}$, are nonzero. These contributions are expected to be dominated by the metal d orbitals. If one neglects the chalcogenide p orbital admixing to the CB, these are the only terms that can explain the spin splitting of the CB, which is found in FP calculations [26,32,36,66,67], and this is the motivation to consider these second-order terms in Ref. [26]. For the ↑ states at the K point, the term $|\Delta_{c,c+1}|^2/(\varepsilon_c - \varepsilon_{c+1})$ predicts a *negative* shift. This would mean that the heavier ↑ band would be lower in energy than the lighter ↓ band. In our DFT calculations, this is indeed the case for WS$_2$ and WSe$_2$, but not for MoS$_2$ and MoSe$_2$. However, from the orbital decomposition of the FP results (see, e.g., Ref. [27]), we know that there is small chalcogenide p-orbital contribution to the CB as well. The X-p orbitals, which have initially been neglected [26,45] in the discussion of the spin splitting in the CB, give rise to the first term in Eqs. (B2b) and (B3b) (the largest weight in the CB comes from the M-d_{z^2} orbitals, but these carry no angular momentum, so they play no role in the SOC). Taking $\Delta_c > 0$ at the K point (the corresponding Bloch wave function is an eigenfunction of $\hat{L}_z$ with positive eigenvalue, see Table IV in Ref. [26]), the contribution of the X-p orbitals to the energy of the ↑ states is *positive*. Therefore, a plausible explanation of the presence or absence of the band crossing in the spin-split CB for MoX$_2$/WX$_2$ materials is that these two contributions compete. Namely, from Eqs. (B2b) and (B3b), it is clear that the X-p orbitals contribute to the spin splitting in first order, whereas remote bands contribute in second order; therefore, it is not obvious which is dominant. It is possible that for MoX$_2$ materials the first, X-p orbital–related term is larger, whereas in the case of WX$_2$, which contains a heavier metal, the second term is larger, explaining the difference between the MoX$_2$ and WX$_2$ materials regarding the energy of the heavier or lighter CB (this possibility has also been mentioned recently in Ref. [36]).

TABLE VII. Parameters appearing in the expressions for g_{vl} and g_{so} for different TMDCs.

	MoS$_2$	WS$_2$	MoSe$_2$	WSe$_2$
$|\gamma_3|$ [eV/Å]	3.01	3.86	2.51	3.32
$2|\Delta_v|$ [eV]	0.146	0.42	0.184	0.456
E_{bg} [eV]	1.85	1.98	1.624	1.736

In addition, the X-p orbital contribution to the CB spin splitting seems to be the simplest way to explain the difference between the spin splitting of MoX_2 and $MoSe_2$: in our DFT calculations, we find that it is larger in $MoSe_2$ ($\Delta_c^{MoSe_2} \approx 23$ meV), which contains a heavier chalcogenide than in MoS_2 ($\Delta_c^{MoS_2} \approx 3$ meV). On the other hand, the above reasoning would suggest that, because of the competition between the two SOC terms of different origins, the splitting in WS_2 ($\Delta_c^{WS_2} \approx 38$ meV) should be larger than in WSe_2 ($\Delta_c^{WSe_2} \approx 46$ meV), which is not the case according to our DFT calculations. This might be related to the larger orbital weight of the M-d orbitals in the relevant bands in the case of WSe_2. In any case, the detailed understanding of the SOC in the CB requires further study.

3. Band-edge shift H_U

The Hamiltonian H_U in Eqs. (B2c) and (B3c) describes the dependence of the band edge on the external electric field. An order-of-magnitude estimate can be obtained by calculating $\zeta_{c,v-2}$ using LDA Kohn-Sham orbitals, generated by the CASTEP code. As one can see from Table VIII, it is a small effect for the electric field values ($E_z \lesssim 10^{-2}$ V/Å), where the perturbation theory should be valid, and therefore we neglect it. We note that, as one can see in Eqs. (B2c) and (B3c), the value of H_U also depends (indirectly) on E_{bg}. The band gap, according to GW calculations [32,68–71], is most likely to be

TABLE VIII.   Band-edge shift H_U in meV, if E_z is expressed in V/Å.

	MoS_2	WS_2	$MoSe_2$	WSe_2
H_U [meV]	$24.6 E_z^2$	$2.4 E_z^2$	$30.3 E_z^2$	$3.0 E_z^2$

underestimated by our DFT-LDA calculations. On the other hand, $\xi_{c,v-2}$ is probably overestimated, because screening is neglected in our perturbative Kohn-Sham-orbital-based calculations. As a consequence, the values shown in Table VIII overestimate the real value of H_U. This conclusion is supported by our preliminary DFT results on the E_z dependence of E_{bg} obtained by the CASTEP code.

The shift of the band edge is, in principle, spin dependent, but as one can see from Eqs. (B2c) and (B3c), this is a higher-order effect and can be safely neglected.

4. Bychkov-Rashba Hamiltonian H_{BR}

Finally, we discuss the Bychkov-Rashba Hamiltonian [Eqs. (B2d) and (B3d)]. It is a sum of several terms, each having the same structure and related to the matrix elements $\xi_{v,c+1}$, $\xi_{v-3,v-1}$, $\xi_{c+1,v-1}$, and $\xi_{c,v-2}$. Using Löwdin partitioning, one finds for the most important term at the K point,

$$\tilde{H}_{BR}^{(1),K} \approx \frac{1}{(\varepsilon_c - \epsilon_v^{\downarrow})(\varepsilon_c - \varepsilon_{c+1})}(\gamma_3^* q_+ \xi_{v,c+1} s_- \Delta_{c,c+1}^* + \gamma_3 q_- \xi_{v,c+1}^* s_+ \Delta_{c,c+1})$$
$$= (\lambda_{BR}^{(1),r} + i\lambda_{BR}^{(1),i})q_+ s_- + (\lambda_{BR}^{(1),r} - i\lambda_{BR}^{(1),i})q_- s_+$$
$$= \lambda_{BR}^{(1),r}(s_x q_x + s_y q_y) + \lambda_{BR}^{(1),i}(s_y q_x - s_x q_y) \tag{B9a}$$

$$= \begin{pmatrix} 0 & (\lambda_{BR}^{(1)})^* q_- \\ \lambda_{BR}^{(1)} q_+ & 0 \end{pmatrix}. \tag{B9b}$$

To make the results more transparent, in the above formula we neglect the spin splittings of the CB and CB + 1, which are much smaller than the splitting of the VB. The product $\gamma_3^* \xi_{v,c+1} \Delta_{c,c+1}^*$ is, in general, a complex number and, therefore, the Bychkov-Rashba coupling constant

$$\lambda_{BR}^{(1)} = \frac{\gamma_3^* \xi_{v,c+1} \Delta_{c,c+1}^*}{(\varepsilon_c - \epsilon_v^{\downarrow})(\varepsilon_c - \varepsilon_{c+1})} \tag{B10}$$

is also complex. By separating the real and imaginary parts of $\lambda_{BR}^{(1)}$, one can write $H_{BR}^{(1),K}$ in the more familiar form shown in Eq. (B9a)).

One can estimate the magnitude of $\lambda_{BR}^{(1)}$ in the following way. As mentioned in Appendix A4, one can calculate the magnitude of $\zeta_{v,c+1}^z$ and the parameter γ_3 using the

band-edge Kohn-Sham orbitals (see Table IX). The band-edge energies $\epsilon_c^{\uparrow,\downarrow}$, $\epsilon_v^{\downarrow}$, and $\varepsilon_{c+1}^{\uparrow,\downarrow}$ are known from DFT-LDA band structure calculations; we have collected their values in Table IX. Unfortunately, the off-diagonal SOC matrix element $\Delta_{c,c+1}$ is not directly given by the DFT calculations. However, information about the weight of the M-d orbitals in each of the bands can be obtained from DFT computations, and, therefore, we can relate this matrix element to Δ_v, because the dominant contribution to the SOC should come from the M-d orbitals. Because the M-d orbital weight in both the CB and the CB + 1 band is similar to the one in the VB, we take $|\Delta_{c,c+1}| \lesssim |\Delta_v|$.

A similar procedure can be performed to estimate the terms proportional to the other nonzero $\xi_{b,b'}$ matrix elements as well. We find that the magnitude of these further terms are significantly smaller than that of $\lambda_{BR}^{(1)}$, mainly because of the prefactors, which are inversely proportional to the product of band-edge energy differences between remote bands. Therefore, as an order-of-magnitude estimate of the

TABLE IX. Parameters appearing in Eq. (B10) for different TMDCs. $\xi_{v,c+1}$ is calculated using DFT-LDA Kohn-Sham orbitals. The other parameters are obtained from DFT-LDA band structure calculations. E_z is in units of V/Å.

	MoS$_2$	WS$_2$	MoSe$_2$	WSe$_2$
$\lvert\xi_{v,c+1}\rvert$ [eV Å]	$0.54E_z$	$0.6E_z$	$0.57E_z$	$0.64E_z$
$\varepsilon_c - \varepsilon_v^{\downarrow}$ [eV]	1.77	1.71	1.54	1.44
$\varepsilon_c - \varepsilon_{c+1}$ [eV]	-1.16	-1.33	-0.925	-1.14

strength of the Bychkov-Rashba SOC, one can just use $\lambda_{\mathrm{BR}}^{(1)}$. Taking values for $\lvert\gamma_3\rvert$ from Table VII and for the other parameters from Table IX, one finally arrives at the results shown in Table III.

The method outlined here most likely overestimates the real values of the Bychkov-Rashba parameters. In addition to the uncertainties in the values of the SOC matrix elements and the γ_i parameters, there are two other sources of error: (i) the calculation of $\zeta_{b,b'}^z$ did not take into account screening effects (see Ref. [47]) and, (ii) according to *GW* calculations, the real band gap is larger then the DFT one, and this affects the energy denominators in the above formulas.

APPENDIX C: EIGENFUNCTIONS OF THE α_- AND α_+ OPERATORS

Considering the functions $g_{a,l}(\rho,\varphi) = e^{il\varphi}\rho^{\lvert l\rvert/2}e^{-\rho/2}M(a,\lvert l\rvert+1,\rho)$, one can show that

$$\hat{\alpha}_- g_{a,l}(\rho,\varphi) = \begin{cases} \frac{a}{\lvert l\rvert+1} g_{a+1,l-1}(\rho,\phi) & l \leq 0, \\ l g_{a,l-1}(\rho,\phi) & l > 0 \end{cases} \quad \text{(C1)}$$

and

$$\hat{\alpha}_+ g_{a,l}(\rho,\varphi) = \begin{cases} l g_{a-1,l+1}(\rho,\varphi) & l < 0, \\ (1-\frac{a}{m+1}) g_{a,l+1}(\rho,\varphi) & l \geq 0. \end{cases} \quad \text{(C2)}$$

To prove these relations, one may use the following identities for the confluent hypergeometric functions:

$$\partial_\rho M(a,b,\rho) = \frac{a}{b}M(a+1,b+1,\rho) \quad \text{(C3)}$$

$$(b-a)M(a,b+1,\rho) = bM(a,b,\rho) - b\partial_\rho M(a,b,\rho), \quad \text{(C4)}$$

$$(b-1)M(a,b-1,\rho) = (b-1)M(a,b,\rho) + \rho\partial_\rho M(a,b,\rho), \quad \text{(C5)}$$

$$(b-1)M(a-1,b-1,\rho) = (b-1-\rho)M(a,b,\rho) + \rho\partial_\rho M(a,b,\rho). \quad \text{(C6)}$$

TABLE X. DFT-LDA lattice parameters.

	MoS$_2$	WS$_2$	MoSe$_2$	WSe$_2$
a_0 [Å]	3.129	3.131	3.253	3.253

APPENDIX D: COMPUTATIONAL DETAILS

The band structure calculations are performed with the VASP code [72] using the LDA. The plane-wave cutoff energy is 600 eV. We use a 12×12 Monkhorst-Pack **k**-point grid in the 2 D plane to relax the geometry and a 24×24 grid to calculate the band structure. The artificial periodicity in the vertical direction is 20 Å. The optimized lattice parameter a_0 for each TMDC is shown in Table X.

The matrix elements of the momentum operator $\hat{p}_\pm$ and the Hamiltonian describing the perpendicular electric field are evaluated within the LDA using the CASTEP code [73] because the necessary plane-wave coefficients of the Kohn-Sham orbitals at the band edges were readily accessible in the output of CASTEP. We use norm-conserving pseudopotentials, a plane-wave cutoff energy of 2177 eV, an artificial periodicity of 15.9 Å in the vertical direction, and a 21×21 Monkhorst-Pack mesh. The optimized lattice parameters are similar to those found in the VASP calculations.

[1] Q. H. Wang, K. Kalantar-Zadeh, A. Kis, J. N. Coleman, and M. S. Strano, *Electronics and Optoelectronics of Two-Dimensional Transition Metal Dichalcogenides*, Nat. Nanotechnol. **7**, 699 (2012).

[2] A. H. Castro Neto, F. Guinea, N. M. R. Peres, K. S. Novoselov, and A. K. Geim, *The Electronic Properties of Graphene*, Rev. Mod. Phys. **81**, 109 (2009).

[3] K. F. Mak, C. Lee, J. Hone, J. Shan, and T. F. Heinz, *Atomically Thin* MoS$_2$: *A New Direct-Gap Semiconductor*, Phys. Rev. Lett. **105**, 136805 (2010).

[4] A. Splendiani, L. Sun, Y. Zhang, T. Li, J. Kim, Ch.-Y. Chim, G. Galli, and F. Wang, *Emerging Photoluminescence in Monolayer* MoS$_2$, Nano Lett. **10**, 1271 (2010).

[5] D. Xiao, G.-B. Liu, W. Feng, X. Xu, and W. Yao, *Coupled Spin and Valley Physics in Monolayers of* MoS$_2$ *and Other Group-VI Dichalcogenides*, Phys. Rev. Lett. **108**, 196802 (2012).

[6] K. F. Mak, K. He, J. Shan, and T. F. Heinz, *Control of Valley Polarization in Monolayer* MoS$_2$ *by Optical Helicity*, Nat. Nanotechnol. **7**, 494 (2012).

[7] H. Zeng, J. Dai, W. Yao, D. Xiao, and X. Cui, *Valley Polarization in* MoS$_2$ *Monolayers by Optical Pumping*, Nat. Nanotechnol. **7**, 490 (2012).

[8] T. Cao, G. Wang, W. Han, H. Ye, Ch. Zhu, J. Shi, Q. Niu, P. Tan, E. Wang, B. Liu, and J. Feng, *Valley-Selective Circular Dichroism of Monolayer Molybdenum Disulphide*, Nat. Commun. **3**, 887 (2012).

[9] G. Sallen, L. Bouet, X. Marie, G. Wang, C. R. Zhu, W. P. Han, Y. Lu, P. H. Tan, T. Amand, B. L. Liu, and B. Urbaszek, *Robust Optical Emission Polarization in* MoS$_2$

Monolayers through Selective Valley Excitation, Phys. Rev. B **86**, 081301 (2012).

[10] H. Zeng, G.-B. Liu, J. Dai, Y. Yan, B. Zhu, R. He, L. Xie, Sh. Xu, X. Chen, W. Yao, and X. Cui, *Optical Signature of Symmetry Variations and Spin-Valley Coupling in Atomically Thin Tungsten Dichalcogenides*, Sci. Rep. **3**, 1608 (2013).

[11] A. M. Jones, H. Yu, N. Ghimire, S. Wu, G. Aivazian, J. S. Ross, J. Yan, B. Zhao, D. Mandrus, D. Xiao, W. Yao, and X. Xu, *Optical Generation of Excitonic Valley Coherence in Monolayer* WSe$_2$, Nat. Nanotechnol. **8**, 634 (2013).

[12] S. Das, H.-Y. Chen, A. V. Penumatcha, and J. Appenzeller, *High-Performance Multilayer* MoS$_2$ *Transistors with Scandium Contacts*, Nano Lett. **13**, 100 (2013).

[13] M. M. Perera, M.-W Lin, H.-J. Chuang, Ch. Wang, Bh. P. Chamlagain, X. Tan, M. M.-Ch. Cheng, D. Tománek, and Z. Zhou, *Improved Carrier Mobility in Few-Layer* MoS$_2$ *Field-Effect Transistors with Ionic-Liquid Gating*, ACS Nano **7**, 4449 (2013).

[14] D. Braga, I. G. Lezama, H. Berger, and A. F. Morpurgo, *Quantitative Determination of the Band Gap of* WS$_2$ *with Ambipolar Ionic Liquid-Gated Transistors*, Nano Lett. **12**, 5218 (2012).

[15] H. Fang, M. Tosun, G. Seol, T. Ch. Chang, K. Takei, J. Guo, and A. Javey, *Degenerate n Doping of Few-Layer Transition Metal Dichalcogendies by Potassium*, Nano Lett. **13**, 1991 (2013).

[16] J.-R. Chen, P. M. Odenthal, A. G. Swartz, G. Ch. Floyd, H. Wen, K. Y. Luo, and R. K. Kawakami, *Control of Schottky Barriers in Single-Layer* MoS$_2$ *Transistors with Ferromagnetic Contacts*, Nano Lett. **13**, 3106 (2013).

[17] H. Yuan, M. S. Bahramy, K. Morimoto, S. Wu, K. Nomura, B.-J. Yang, H. Shimotani, R. Suzuki, M. Toh, Ch. Kloc, X. Xu, R. Arita, N. Nagaosa, and Y. Iwasa, *Zeeman-Type Spin Splitting Controlled by an Electric Field*, Nat. Phys. **9**, 563 (2013).

[18] B. W. H. Baugher, H. O. H. Churchill, Y. Yang, and P. Jarillo-Herrero, *Optoelectronics with Electrically Tunable PN Diodes in a Monolayer Dichalcogenide*, arXiv:1310.0452.

[19] B. Radisavljević and A. Kis, *Mobility Engineering and a Metal-Insulator Transition in Monolayer* MoS$_2$, Nat. Mater. **12**, 815 (2013).

[20] A. T. Neal, H. Liu, J. Gu, and P. D. Ye, *Magnetotransport in* MoS$_2$: *Phase Coherence, Spin-Orbit Scattering and the Hall Factor*, ACS Nano **7**, 7077 (2013).

[21] D. Loss and D. P. DiVincenzo, *Quantum Computation with Quantum Dots*, Phys. Rev. A **57**, 120 (1998).

[22] J. S. Ross, S. Wu, H. Yu, N. J. Ghimire, A. M. Jones, G. Aivazian, J. Yan, D. G. Mandrus, D. Xiao, W. Yao, and X. Xu, *Electrical Control of Neutral and Charged Excitons in a Monolayer Semiconductor*, Nat. Commun. **4**, 1474 (2013).

[23] W. Bao, X. Cai, D. Kim, K. Sridhara, and M. S. Fuhrer, *High-Mobility Ambipolar* MoS$_2$ *Field-Effect Transistors: Substrate and Dielectric Effects*, Appl. Phys. Lett. **102**, 042104 (2013).

[24] J. Klinovaja and D. Loss, *Spintronics in* MoS$_2$ *Monolayer Quantum Wires*, Phys. Rev. B **88**, 075404 (2013).

[25] Y. Song and H. Dery, *Transport Theory of Monolayer Transition-Metal Dichalcogenides through Symmetry*, Phys. Rev. Lett. **111**, 026601 (2013).

[26] A. Kormányos, V. Zólyomi, N. D. Drummond, P. Rakyta, G. Burkard, and V. I. Fal'ko, *Monolayer* MoS$_2$: *Trigonal Warping, the* Γ *Valley and Spin-Orbit Coupling Effects*, Phys. Rev. B **88**, 045416 (2013).

[27] E. Cappelluti, R. Roldán, J. A. Silva-Guillén, P. Ordejón, and F. Guinea, *Tight-Binding Model and Direct-Gap/ Indirect-Gap Transition in Single-Layer and Multilayer* MoS$_2$, Phys. Rev. B **88**, 075409 (2013).

[28] A. Ramasubramaniam (private communication).

[29] Compare, e.g., Fig. 3 in Ref. [70] and Fig. 1 in Ref. [32].

[30] W. Zhao, Z. Ghorannevis, L. Chu, M. Toh, Ch. Kloc, P.-H. Tan, and G. Eda, *Evolution of Electronic Structure in Atomically Thin Sheets of* WS$_2$ *and* WSe$_2$, ACS Nano **7**, 791 (2013).

[31] H. R. Gutiérrez, N. Perea-López, A. L. Elías, A. Berkdemir, B. Wang, R. Lv, F. López-Urías, V. H. Crespi, H. Terrones, and M. Terrones, *Extraordinary Room-Temperature Photoluminescence in Triangular* WS$_2$ *Monolayers*, Nano Lett. **13**, 3447 (2013).

[32] T. Cheiwchanchamnangij and W. R. L. Lambrecht, *Quasiparticle Band Structure Calculation of Monolayer, Bilayer, and Bulk* MoS$_2$, Phys. Rev. B **85**, 205302 (2012).

[33] The fitting was performed in a range around the K point, which corresponds to ≈6% of the Γ-K distance.

[34] L. Wang and M. W. Wu, *Intrinsic Electron Spin Relaxation due to the D'yakonov-Perel' Mechanism in Monolayer* MoS$_2$, arXiv:1305.3361.

[35] H. Ochoa, F. Guinea, and V. I. Fal'ko, *Spin Memory and Spin-Lattice Relaxation in Two-Dimensional Hexagonal crystals*, Phys. Rev. B **88**, 195417 (2013).

[36] G.-B. Liu, W.-Y. Shan, Y. Yao, W. Yao, and D. Xiao, *Three-Band Tight-Binding Model for Monolayers of Group-VIB Transition Metal Dichalcogenides*, Phys. Rev. B **88**, 085433 (2013).

[37] M. Koshino and T. Ando, *Anomalous Orbital Magnetism in Dirac-Electron Systems: Role of Pseudospin Paramagnetism*, Phys. Rev. B **81**, 195431 (2010).

[38] P. Recher, J. Nilsson, G. Burkard, and B. Trauzettel, *Bound States and Magnetic Field-Induced Valley Splitting in Gate-Tunable Graphene Quantum Dots*, Phys. Rev. B **79**, 085407 (2009).

[39] L. M. Zhang, M. M. Fogler, and D. P. Arovas, *Magneto-electric Coupling, Berry Phase, and Landau Level Dispersion in a Biased Bilayer Graphene*, Phys. Rev. B **84**, 075451 (2011).

[40] H. Rostami, A. G. Moghaddam, and R. Asgari, *Effective Lattice Hamiltonian for Monolayer* MoS$_2$: *Tailoring Electronic Structure with Perpendicular Electric and Magnetic Fields*, Phys. Rev. B **88**, 085440 (2013).

[41] F. Rose, M. O. Goerbig, and F. Piéchon, *Spin-and Valley-Dependent Magneto-Optical Properties of* MoS$_2$, Phys. Rev. B **88**, 125438 (2013).

[42] T. Cai, Sh. A. Yang, X. Li, F. Zhang, J. Shi, W. Yao, and Q. Niu, *Magnetic Control of the Valley Degree of Freedom of Massive Dirac Fermions with Application to Transition Metal Dichalcogenides*, Phys. Rev. B **88**, 115140 (2013).

[43] M. S. Dresselhaus, G. Dresselhaus, and A. Jorio, *Group Theory* (Springer-Verlag, Berlin, 2008).

[44] Y. A. Bychkov and E. I. Rasbha, *Properties of a 2D Electron Gas with Lifted Spectral Degeneracy*, JETP Lett. **39**, 78 (1984)., *Oscillatory Effects and the Magnetic Susceptibility of Carriers in Inversion Layers*, J. Phys. C **17**, 6039 (1984).

[45] H. Ochoa and R. Roldán, *Spin-Orbit-Mediated Spin Relaxation in Monolayer* MoS_2, Phys. Rev. B **87**, 245421 (2013).

[46] S. Vajna, E. Simon, A. Szilva, K. Palotás, B. Újfalussy, and L. Szúnyogh, *Higher-Order Contributions to the Rashba-Bychkov Effect with Application to the* Bi/Ag(111) *Surface Alloy*, Phys. Rev. B **85**, 075404 (2012).

[47] N. D. Drummond, V. Zólyomi, and V. I. Fal'ko, *Electrically Tunable Band Gap in Silicene*, Phys. Rev. B **85**, 075423 (2012).

[48] S. Konschuh, M. Gmitra, D. Kochan, and J. Fabian, *Theory of Spin-Orbit Coupling in Bilayer Graphene*, Phys. Rev. B **85**, 115423 (2012).

[49] T. Koga, J. Nitta, T. Akazaki, and H. Takayanagi, *Rashba Spin-Orbit Coupling Probed by the Weak Antilocalization Analysis in* InAlAs/InGaAs/InAlAs *Quantum Wells as a Function of Quantum Well Asymmetry*, Phys. Rev. Lett. **89**, 046801 (2002).

[50] A. M. Gilbertson, M. Fearn, J. H. Jefferson, B. N. Murdin, P. D. Buckle, and L. F. Cohen, *Zero-Field Spin Splitting and Spin Lifetime in* $n-InSb/In_{1-x}Al_xSb$ *Asymmetric Quantum Well Heterostructures*, Phys. Rev. B **77**, 165335 (2008).

[51] J. Milton Pereira, Jr., P. Vasilopoulos, and F. M. Peeters, *Tunable Quantum Dots in Bilayer Graphene*, Nano Lett. **7**, 946 (2007).

[52] X. L. Liu, D. Hug, and L. M. K. Vandersypen, *Gate-Defined Graphene Double Quantum Dot and Excited State Spectroscopy*, Nano Lett. **10**, 1623 (2010).

[53] M. T. Allen, J. Martin, and A. Yacoby, *Gate-Defined Quantum Confinement in Suspended Bilayer Graphene*, Nat. Commun. **3**, 934 (2012).

[54] S. Nadj-Perge, S. M. Frolov, E. P. A. M. Bakkers, and L. P. Kouwenhoven, *Spin-Orbit Qubit in a Semiconductor Nanowire*, Nature (London) **468**, 1084 (2010).S. Nadj-Perge, V. S. Pribiag, J. W. G. van den Berg, K. Zuo, S. R. Plissard, E. P. A. M. Bakkers, S. M. Frolov, and L. P. Kouwenhoven, *Spectroscopy of Spin-Orbit Quantum Bits in Indium Antimonide Nanowires*, Phys. Rev. Lett. **108**, 166801 (2012).

[55] G. A. Intronati, P. I. Tamborenea, D. Weinmann, and R. A. Jalabert, *Spin-Orbit Effects in Nanowire-Based Wurtzite Semiconductor Quantum Dots*, Phys. Rev. B **88**, 045303 (2013).

[56] I. L. Aleiner and V. I. Fal'ko, *Spin-Orbit Coupling Effects on Quantum Transport in Lateral Semiconductor Dots*, Phys. Rev. Lett. **87**, 256801 (2001).

[57] E. Tsitsishvili, G. S. Lozano, and A. O. Gogolin, *Rashba Coupling in Quantum Dots: An Exact Solution*, Phys. Rev. B **70**, 115316 (2004).

[58] See, e.g., http://dlmf.nist.gov/13.2.

[59] S. Schnez, K. Ensslin, M. Sigrist, and T. Ihn, *Analytic Model of the Energy Spectrum of a Graphene Quantum Dot in a Perpendicular Magnetic Field*, Phys. Rev. B **78**, 195427 (2008).

[60] P. Recher and B. Trauzettel, *Quantum Dots and Spin Qubits in Graphene*, Nanotechnology **21**, 302001 (2010).

[61] K. Flensberg and C. M. Marcus, *Bends in Nanotubes Allow Electric Spin Control and Coupling*, Phys. Rev. B **81**, 195418 (2010).

[62] A. Scholz, T. Stauber, and J. Schliemann, *Plasmons and Screening in a Monolayer of* MoS_2, Phys. Rev. B **88**, 035135 (2013).

[63] K. Kośmider, J. W. González, and J. Fernández-Rossier, *Large Spin Splitting in the Conduction Band of Transition Metal Dichalcogenide Monolayers*, Phys. Rev. B **88**, 245436 (2013).

[64] R. Winkler, *Spin-Orbit Coupling Effects in Two-Dimensional Electron and Hole Systems* (Springer-Verlag, Berlin, 2003).

[65] L. M. Roth, *g Factor and Donor Spin-Lattice Relaxation for Electrons in Germanium and Silicon*, Phys. Rev. **118**, 1534 (1960).

[66] K. Kośmider and J. Fernández-Rossier, *Electronic Properties of the* $MoS_2 - WS_2$ *Heterojunction*, Phys. Rev. B **87**, 075451 (2013).

[67] Z. Y. Zhu, Y. C. Cheng, and U. Schwingenschlögl, *Giant Spin-Orbit-Induced Spin Splitting in Two-Dimensional Transition-Metal Dichalcogenide Semiconductors*, Phys. Rev. B **84**, 153402 (2011).

[68] A. Ramasubramaniam, *Large Excitonic Effects in Monolayers of Molybdenum and Tungsten Dichalcogenides*, Phys. Rev. B **86**, 115409 (2012).

[69] H.-P. Komsa and A. V. Krasheninnikov, *Effects of Confinement and Environment on the Electronic Structure and Exciton Binding Energy of* MoS_2 *from First Principles*, Phys. Rev. B **86**, 241201(R) (2012).

[70] H. Shi, H. Pan, Y.-W. Zhang, and B. I. Yakobson, *Quasiparticle Band Structures and Optical Properties of Strained Monolayer* MoS_2 *and* WS_2, Phys. Rev. B **87**, 155304 (2013).

[71] Y. Liang, Sh. Huang, R. Soklaski, and Li Yang, *Quasiparticle Band-Edge Energy and Band Offsets of Monolayer of Molybdenum and Tungsten Chalcogenide*, Appl. Phys. Lett. **103**, 042106 (2013).

[72] G. Kresse and J. Furthmüller, *Efficient Iterative Schemes for Ab Initio Total-Energy Calculations Using a Plane-Wave Basis Set*, Phys. Rev. B **54**, 11169 (1996).

[73] S. J. Clark, M. D. Segall, C. J. Pickard, P. J. Hasnip, M. I. J. Probert, K. Refson, and M. C. Payne, *First-Principles Methods Using CASTEP*, Z. Kristallogr. **220**, 567 (2005).